

## The impact of coherent large-scale vortices generated by helix active wake control on the recovery process of wind turbine wakes

Gutknecht, J.; Taschner, E.; Coquelet, M.; Viré, A.; van Wingerden, J. W.

**DOI**

[10.1063/5.0278687](https://doi.org/10.1063/5.0278687)

**Publication date**

2025

**Document Version**

Final published version

**Published in**

Physics of Fluids

**Citation (APA)**

Gutknecht, J., Taschner, E., Coquelet, M., Viré, A., & van Wingerden, J. W. (2025). The impact of coherent large-scale vortices generated by helix active wake control on the recovery process of wind turbine wakes. *Physics of Fluids*, 37(6), Article 067162. <https://doi.org/10.1063/5.0278687>

**Important note**

To cite this publication, please use the final published version (if applicable).  
Please check the document version above.

**Copyright**






Other than for strictly personal use, it is not permitted to download, forward or distribute the text or part of it, without the consent of the author(s) and/or copyright holder(s), unless the work is under an open content license such as Creative Commons.

**Takedown policy**

Please contact us and provide details if you believe this document breaches copyrights.  
We will remove access to the work immediately and investigate your claim.

RESEARCH ARTICLE | JUNE 30 2025

## The impact of coherent large-scale vortices generated by helix active wake control on the recovery process of wind turbine wakes

J. Gutknecht ; E. Taschner ; M. Coquelet ; A. Viré ; J. W. van Wingerden 



*Physics of Fluids* 37, 067162 (2025)

<https://doi.org/10.1063/5.0278687>



### Articles You May Be Interested In

Numerical study on the impact of structural flexibility and platform motions on the dynamic behaviors and wake characteristics of floating offshore wind turbine

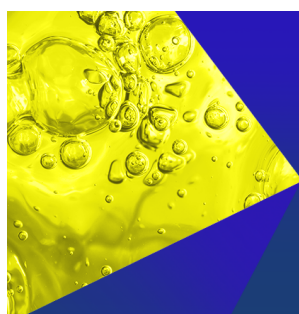
*Physics of Fluids* (June 2025)

On the absence of asymmetric wakes for periodically plunging finite wings

*Physics of Fluids* (July 2014)

A numerical investigation of wake recovery for an H- and X-shaped vertical-axis wind turbine with wake control strategies

*Physics of Fluids* (December 2024)



**Physics of Fluids**  
Special Topics  
Open for Submissions

[Learn More](#)

# The impact of coherent large-scale vortices generated by helix active wake control on the recovery process of wind turbine wakes

Cite as: Phys. Fluids **37**, 067162 (2025); doi: [10.1063/5.0278687](https://doi.org/10.1063/5.0278687)

Submitted: 1 May 2025 · Accepted: 5 May 2025 ·

Published Online: 30 June 2025



View Online



Export Citation



CrossMark

J. Gutknecht,<sup>1,a)</sup> E. Taschner,<sup>1</sup> M. Coquelet,<sup>1</sup> A. Viré,<sup>2</sup> and J. W. van Wingerden<sup>1</sup>

## AFFILIATIONS

<sup>1</sup>Delft Center for Systems and Control, Delft University of Technology, Mekelweg 2, 2628 CD Delft, The Netherlands

<sup>2</sup>Wind Energy Section, Delft University of Technology, Kluyverweg 1, 2629 HS Delft, The Netherlands

<sup>a)</sup>Author to whom correspondence should be addressed: [j.gutknecht@tudelft.nl](mailto:j.gutknecht@tudelft.nl)

## ABSTRACT

Within a wind farm, each wind turbine extracts kinetic energy from the flow to convert it into electric energy. Unavoidably, this reduces the downstream availability of kinetic energy, diminishing the power generation of turbines operating in the waked region. These wake-induced power losses cumulate throughout the wind farm, posing a risk to its economic feasibility. One method that mitigates these power losses is helix active wake control. By leveraging individual blade pitch control, it induces an uneven thrust distribution over the rotor plane, which rotates either in clockwise (CW) or counterclockwise (CCW) direction around the rotor center. The wake deforms into a helical shape that recovers faster than the wake of a conventionally controlled turbine and thereby increases the total generated power. Notably, the CCW helix consistently outperforms the CW helix across all available studies. This work investigates the physical principles underlying these wake recovery enhancements using large eddy simulations (LES) of a wind turbine exposed to laminar, uniform flow. We observe a spatially coherent helical vortex structure in the wake boundary, which actively transports mean kinetic energy into the wake and, therefore, poses a fundamental contributor to the wake recovery enhancement. The opposing rotational directions of CW and CCW helices result in distinct interactions of the helical vortex with the hub vortex, leading to different wake recovery mechanisms. In the investigated laminar inflow, the CCW helix has transported 44.8% more mean kinetic energy into the wake than the CW helix up to a streamwise position of 5D, explaining their differing efficacies observed in previous studies.

© 2025 Author(s). All article content, except where otherwise noted, is licensed under a Creative Commons Attribution-NonCommercial 4.0 International (CC BY-NC) license (<https://creativecommons.org/licenses/by-nc/4.0/>). <https://doi.org/10.1063/5.0278687>

## I. INTRODUCTION

Wind energy is considered a fundamental pillar of the transition to a sustainable energy supply in many countries worldwide. Thereby, several economic effects motivate the arrangement of multiple turbines in close spatial proximity to so-called wind farms.<sup>1</sup> Apart from logistic effects such as the shared use of infrastructure and reduced cable length, a strong motivation for densely spaced wind farms is the maximization of the energy density, which describes the energy harvested within the available surface area. However, these effects cannot be exploited indefinitely due to aerodynamic interactions between the turbines.<sup>2</sup> Each turbine extracts kinetic energy from the wind and converts it to electrical energy, leaving a deficit of kinetic energy in the flow in its downstream region, the so-called wake. This negatively affects the power production of a turbine operating in the wake of an upstream one since it has less kinetic energy available to convert to

electric energy. These power losses can range up to 40% compared to a turbine operating in the free wind speed.<sup>2</sup>

To further increase the power density of a wind farm and thereby facilitate the economic viability of wind energy, the community devised various methodologies to mitigate wake effects in the past years.<sup>3</sup> One class of these methodologies aims to manipulate the wake through control measures at the upstream turbine. A first control approach was statically derating upstream turbines to reduce their energy extraction from the flow to generate less pronounced wakes.<sup>4</sup> The second approach is to misalign the upstream turbines with the incoming wind direction to induce a force in the crossflow direction on the flow. This causes a lateral displacement of the wake, which can be used to steer it away from downstream turbines.<sup>5–8</sup> A third type is active wake control, which tries to accelerate the recovery of the wake deficit with dynamic control actions at the upstream turbine. The first

relevant successes in that field were achieved by the so-called pulse, which sinusoidally varies the thrust force of the upstream turbines, using collective pitch actuation. This accelerates the recovery of the wake, translating to power gains of about 5% in a  $4 \times 4$  wind farm in a turbulent flow.<sup>9,10</sup>

The power gains obtained with the pulse come with increased variations of the generated power. This issue is addressed by a close relative to the pulse named helix active wake control or just helix, which was first presented by Frederik *et al.*<sup>11</sup> While the pulse only perturbs the temporal uniformity of the energy extraction from the flow, the helix additionally induces a spatial perturbation. Therefore, it increases the thrust force on one half-plane of the rotor and reduces it on the other. The spatially nonuniform thrust distribution rotates around the rotor center, either clockwise (CW)—aligned with rotor rotation and opposing wake swirl—or counterclockwise (CCW)—opposing rotor rotation and aligning with wake swirl, as viewed from upstream in streamwise direction. This perturbation is created by sinusoidally varying the individual blade pitch angle over the rotor plane. As a result, the wake deforms into the name-giving helical shape as visualized in Fig. 1 using velocity contour surfaces obtained from large-eddy-simulation (LES) of one turbine in uniform laminar flow. Several studies have investigated the effectiveness of both helix types in different experimental and numerical environments. The first study in LES presented by Frederik *et al.*<sup>11</sup> reported a gain of 7.5% of the power generated by a two-turbine wind farm in a flow with 5% turbulence intensity using the CCW helix. In contrast, the CW helix only achieved power gains of 2.5%. Numerous studies, performed numerically and experimentally, reproduced the positive effects of the helix on the total power generated by two aligned turbines,<sup>12–14</sup> even though with a high variation of the absolute gains. The overall trend is that with increasing pitch amplitude, the power losses at the actuated turbine increase. These losses can be compensated by increasing power gains at the downstream turbine such that the overall generated power profits from the helix. For instance, Taschner *et al.*<sup>12</sup> observed a total power gain of 3.1% when the upstream turbine applies the helix with a pitch amplitude of  $2^\circ$  compared to both turbines operating in baseline control. Further studies using LES,<sup>15</sup> a vortex particle-mesh method<sup>16</sup> or wind tunnel experiments<sup>13,17,18</sup> also confirm the superior performance of the CCW helix compared to the CW helix.

In addition to the rotational direction, also the excitation frequency, usually expressed by the Strouhal number  $St$ , and the amplitude of the pitch angle actuation were found to impact the efficacy of

the helix. Throughout the available literature, the optimal  $St$  ranges between 0.25 and 0.47 and may even differ between CW and CCW helix.<sup>13,17,18</sup> The wake recovery enhancement profits from larger pitch actuation amplitudes; however, they also come at the cost of increased damage equivalent loads (DEL) in several turbine components, in particular, the blade root flapwise loads and the pitch bearings. In particular, the actuated turbine suffers from the increased DEL, but they are also notable at the waked turbine.<sup>12,19</sup>

The results described above motivated several studies focusing on the underlying mechanisms that enhance the wake recovery when applying the helix. First, explanations were searched in a manipulation of the tip vortices. Van der Hoek *et al.*<sup>17</sup> observed a variation in the tip vortex size and strength in particle image velocimetry (PIV) measurements. These variations accelerate the leapfrogging of neighboring vortices, leading to an earlier destabilization of the wake than in the baseline. The wind tunnel experiments of Mühle *et al.*<sup>18</sup> performed with a fast-response five-hole pressure probe relate the faster wake recovery to a radial meandering of the tip vortices, causing them to interact faster and thus shortening their shielding effects.

However, the impact of helix active wake control goes beyond the effect on the tip vortices. A comprehensive numerical study of the helix is given by Korb *et al.*,<sup>20</sup> which relates the increase in kinetic energy in the wake to two effects. First, in the near wake an accelerated wake transition increases the mixing of the wake with the surrounding flow, and second, in the far wake, the wake gets increasingly deflected in the lateral direction, steering the wake core away from a downstream turbine. In this region, the wake cross section adapts to a kidney shape that reminds of the wake behind a yaw-misaligned turbine.<sup>21</sup>

While Korb *et al.*<sup>20</sup> relate the crossflow deflection of the wake to a radial force in the near wake, Coquelet *et al.*<sup>16</sup> quantify this force to be about 1% of the rotor-normal thrust force. This small magnitude challenges its role as the sole driver of wake deflection, suggesting that additional mechanisms may contribute to the observed wake behavior. Instead, they observe two vorticity lobes in the near wake, eventually forming a system of co-rotating vortices in the far wake, creating the kidney-shaped wake. This was not observed with a static force perturbation, implying that the dynamic nature of the helix perturbation is crucial to trigger the wake re-energizing mechanisms. Brown *et al.*<sup>22</sup> relate the increased wake recovery achieved by wake mixing strategies, including the CCW helix, in low turbulence and high veer to increased turbulent entrainment, highlighting the relevance of coherent structures.

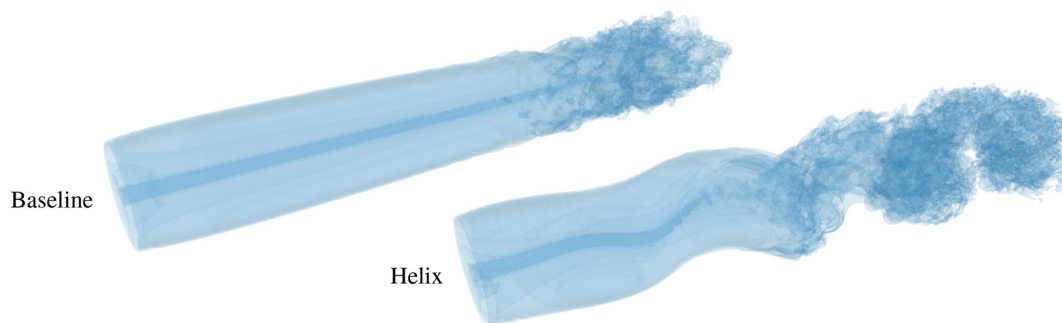


**FIG. 1.** Wakes of a conventionally controlled turbine (baseline) and a turbine applying helix active wake control in counterclockwise direction (CCW) as isosurfaces of the streamwise velocity component  $u_x$ .



Similar counter-rotating vortex structures and a kidney-shaped wake cross section in the far wake were observed by Gutknecht *et al.*<sup>23</sup> in PIV experiments of a simplified helix porous disk model. This model mimics the helix perturbation with a non-uniform porosity distribution, which is rotated at the helix-typical Strouhal numbers. These vortex features exist despite the absence of blade-created phenomena such as a radial force, tip vortices, hub vortex, and swirl, implying that the governing trigger for the helix roots in the thrust force perturbation rather than in the not-modeled blade-related phenomena.

Another perspective to explain the helix roots in the excitation of unstable modes. Muscari *et al.*<sup>15</sup> were the first to investigate spatial coherence in helix wakes by performing a physics-informed dynamic mode decomposition (piDMD). The dominant modes are helically shaped and related to the excitation frequency and its harmonics. Exploiting that coherence, Gutknecht *et al.*<sup>24</sup> developed a data-driven helix model that is capable of reconstructing the helix at different wind speeds by scaling the dynamic modes obtained from one single LES simulation at constant wind speed.

Later, Cheung *et al.*<sup>25</sup> relate various active wake control strategies, among others, the CW and CCW helix, to modal wake instabilities by performing a proper orthogonal decomposition (POD) on LES data. They observe that each wake control strategy triggers a characteristic set of unstable modes that gain energy as they advect downstream into the wake. In the laminar non-sheared inflow, the CCW helix was found to trigger the most unstable mode.

Each of the aforementioned studies contributes to understanding specific characteristics of helix active wake control, providing a well-founded overview of the key aspects. Nevertheless, several research questions remain unresolved. In particular, the physical mechanisms triggered by helix active wake control to enhance the mean kinetic energy in the wake to accelerate its recovery, and the different effectiveness of the CW and CCW helix still lack a causal explanation. This work contributes to closing these gaps of knowledge by the following.

- (1) Identifying and quantifying a system of spatially coherent large-scale vortices with distinct properties in CW and CCW helix.
- (2) Establishing these vortex structures as a fundamental contributor to the wake recovery enhancements achieved with helix active wake control by relating them to the transport of mean kinetic energy into the wake.
- (3) Explaining the higher efficacy of the CCW helix than the CW helix by demonstrating that the CW helix transports less mean kinetic energy into the wake than the CCW helix.

To that end, we isolate the effect of the helix on the wake by performing LES of a single turbine in laminar, uniform inflow. This facilitates the identification of the mechanism triggered by the helix in the wake. We consider three configurations of turbines: one controlled conventionally, one applying CW, and one applying CCW helix active wake control.

The remainder of the paper presents the numerical setup and the flow analysis in Sec. II, followed by the presentation of the observed flow phenomena, including the system of coherent vortices and its effect on the transport of kinetic energy into the wake in Sec. III. The paper concludes by integrating the findings into the current state of the art regarding the helix active wake control in Sec. IV.

## II. METHODOLOGY

The first part of this section presents the helix active wake control scheme, followed by a description of the numerical setup used to

generate the flow field data. The third part describes the post-processing routine, designed to provide deeper insights into the wake recovery mechanisms triggered by the helix approach.

### A. Helix active wake controller

Each wind turbine blade exerts a force on the flow, with one component in azimuthal and one in rotor-normal direction. The azimuthal component creates the torque, which drives the generator to produce electrical power. The rotor-normal component, often referred to as thrust  $F_T$ , is responsible for the deceleration of the flow. A conventionally controlled wind turbine seeks to maximize its generated power, by extracting the same amount of energy from the flow at each azimuthal position, assuming a uniform, laminar inflow. Therefore, the blades exert the same force profile  $F_{BL}(r)$  on the flow along their radius  $r$  at each azimuthal position. Thus, the flow experiences a point-symmetric energy extraction at the rotorplane, leading to a symmetric wake that swirls in the counterclockwise direction against the clockwise rotation of the rotor. Helix active wake control breaks that point symmetry by amplifying the deceleration of the flow on one side of the rotor and reducing it on the other side. Therefore, it superimposes a perturbation  $\tilde{F}_{T,Helix}$  onto the symmetric baseline thrust such that the total thrust assembles as

$$F_{T,Helix}(r, \psi, t) = F_{T,BL}(r) + \tilde{F}_{T,Helix}(r, \psi, t). \quad (1)$$

This force perturbation varies in azimuthal direction  $\psi$  and over time  $t$  to extract the energy from the flow in a non-uniform, unsteady manner. More specifically,  $\tilde{F}_{T,Helix}(r, \psi, t)$  increases the thrust force on one half-plane of the rotor and decreases it on the other half-plane. Additionally, this force pattern rotates either aligned with the wake swirl in CCW direction or against it in CW direction. The non-dimensional Strouhal number  $St$  expresses its rotational frequency  $f_e$  as

$$St = \frac{f_e D}{u_\infty}, \quad (2)$$

where  $D$  is the rotor diameter, and  $u_\infty$  is the free wind speed. The Strouhal number  $St$  was found to govern the efficacy of helix active wake control, reaching optimal performance in the range of  $0.25 \leq St \leq 0.47$ .<sup>13,18</sup> The azimuthal force component experiences a similar perturbation. However, this component is by orders of magnitude smaller than the thrust and, therefore, less relevant for generating the helix.<sup>16</sup>

The flow reacts to this force perturbation with an uneven deceleration over the rotor plane. As the perturbed flow propagates downstream, the perturbation grows and deforms the wake into a name-giving helical shape that spirals either in CW or CCW direction as shown in Fig. 1.

The unsteady force perturbation is created by leveraging individual pitch control (IPC) to excite the pitch angle  $\beta$  of the blades individually. As visualized in Fig. 2, the blades increase  $\beta$  when they swipe through one half-plane and decrease  $\beta$  on the other half-plane. This causes a sinusoidal variation of the angle of attack at the blades, which translates to a variation of the blade forces. A CCW rotation of  $\tilde{F}_{T,Helix}(\psi, t)$  is induced by pitching the blades faster than the rotational velocity of the rotor  $\omega_r$ , a slower pitching than  $\omega_r$  results in a CW

rotation. Consequently, the pitch angle time-series  $\beta_b(t)$  of each individual blade  $b$  can be expressed as

$$\begin{aligned} \text{CW: } \beta_b(t) &= \beta_{BL} + \hat{\beta} \sin[(\omega_r - \omega_e)t + \psi_{0,b}], \\ \text{CCW: } \beta_b(t) &= \beta_{BL} + \hat{\beta} \sin[(\omega_r + \omega_e)t + \psi_{0,b}], \end{aligned} \quad (3)$$

with  $b = \{1, 2, 3\}$  for a three-bladed wind turbine,  $\beta_{BL}$  being the baseline pitch angle,  $\hat{\beta}$  being the amplitude of the pitch actuation,  $\omega_e = 2\pi f_e$  being the excitation angular velocity, and  $\psi_{0,b}$  being the initial azimuthal position of the blade.

This IPC scheme is implemented in the turbine controller using a multiblade coordinate transform (MBC) as described in detail in Frederik *et al.*<sup>11</sup>

## B. Data generation with large eddy simulations

This study aims to understand the mechanisms triggered by helix active wake control to accelerate the wake recovery. Serving this purpose, the simulation setup presented in this section is not intended to represent real-world atmospheric conditions, including turbulence, shear, and veer. Instead, it isolates the effect of the helix actuation on the wake from other effects that might arise from atmospheric turbulence, tower shadow, or shear. Following that intention, we simulate the wake of a single turbine exposed to laminar inflow in three different control scenarios: one conventional greedy control regime (Baseline), one using the helix active wake control in CW direction

(CW), and one in CCW direction (CCW). The simulation setup is summarized in Table I.

We expose the turbine to a laminar uniform inflow with a velocity of  $u_\infty = 9 \text{ ms}^{-1}$ , similar to the inflow conditions used by Frederik *et al.*<sup>11</sup> This wind speed lies in controller region II, where the turbine extracts the maximum energy from the flow by tracking the optimal power coefficient  $C_p$ .<sup>26</sup> In control regions related to higher wind speeds, the turbine switches to tracking the nominal power, which implies a reduced energy extraction from the flow. Consequently, in region II, active wake control methods promise the highest increases in wind farm efficiency since the waked turbine can harvest all the additional kinetic energy. In these conditions, the turbine operates with the optimal Tip Speed Ratio (TSR) of 7.55, which corresponds to a rotational speed of 10.3 rpm.

The flow around the turbine is simulated using the wind turbine and wind farm simulation toolbox *AMR-Wind*,<sup>27,28</sup> which couples the incompressible Navier–Stokes solver *AMRreX* to the multi-physics wind turbine simulation tool *OpenFAST*.<sup>29</sup> It solves the LES formulation of the incompressible Navier–Stokes equations and a transport equation for potential temperature. The governing equations in Cartesian coordinates, using Einstein notation, are

$$\begin{aligned} \frac{\partial \tilde{u}_j}{\partial x_j} &= 0, \\ \frac{\partial \tilde{u}_i}{\partial t} + \frac{\partial \tilde{u}_i \tilde{u}_j}{\partial x_j} &= -\frac{1}{\rho} \frac{\partial \tilde{p}}{\partial x_i} - \frac{\partial \tau_{ij}}{\partial x_j} + \nu \frac{\partial^2 \tilde{u}_i}{\partial x_j \partial x_j} + C_i + B_i + F_i, \\ \frac{\partial \tilde{\theta}}{\partial t} + \frac{\partial \tilde{u}_j \tilde{\theta}}{\partial x_j} &= -\frac{\partial \tau_{\theta j}}{\partial x_j} + \frac{\nu}{\text{Pr}} \frac{\partial^2 \tilde{\theta}}{\partial x_j \partial x_j}, \end{aligned} \quad (4)$$

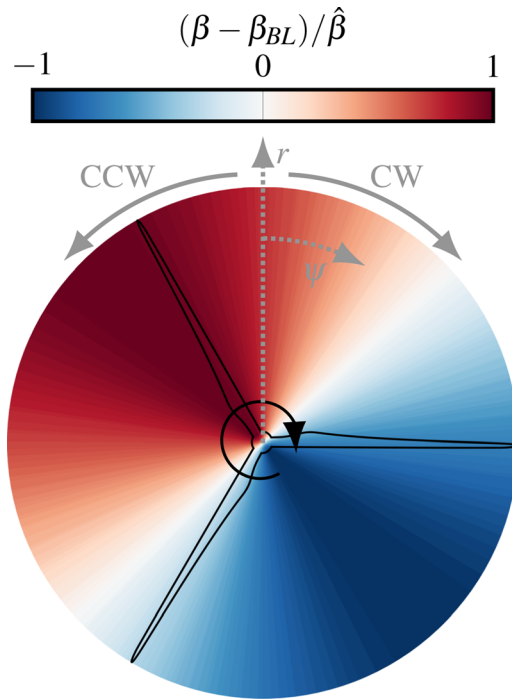


**FIG. 2.** Schematic representation of the pitch angle perturbation  $\beta - \beta_{BL}$ , normalized by the maximum pitch amplitude  $\hat{\beta}$  over the rotor plane induced by the helix at one phase instance. While the rotor always rotates in the CW direction, the perturbation rotates in the CW direction for the CW helix and in CCW direction for the CCW helix, as indicated by the gray arrows. The gray dotted arrows indicate the orientation of the radial direction  $r$  and the azimuthal direction  $\psi$ .

**TABLE I.** Overview of the simulation setup.

Variable		Value
Turbine		NREL 5 MW
Rotor diameter	$D$	126 m
Inflow velocity	$u_\infty$	$9 \text{ ms}^{-1}$
Inflow turbulence intensity	$Ti$	0
Rotational speed	$\omega_r$	10.3 rpm
Tip Speed Ratio	$\text{TSR} = \frac{\omega_r R}{u_\infty}$	7.55
Domain size	$L_x \times L_y \times L_z$	$19 \times 12 \times 12 \text{ D}^3$
Finest grid size	$\Delta x_4$	1.57 m
Coarsest grid size	$\Delta x_0$	25.6 m
Number of grid cells	$N_{\text{cells}}$	$162 \times 10^6$
Timestep	$\Delta t$	0.02 s
CFL at blade tip	$\text{CFL}_{\text{tip}} = \frac{u_{\text{tip}} \Delta t}{\Delta x_4}$	0.88
Strouhal number	$St$	0.3
Helix excitation period	$T_e$	46.66 s
Helix blade pitch amplitude	$\hat{\beta}$	$3^\circ$
Dynamic viscosity	$\mu$	$1.872 \times 10^{-5} \text{ kg(ms)}^{-1}$
Reynolds number	$Re = \frac{\rho u_\infty D}{\mu}$	$74 \times 10^6$

where, following the common LES formulation,  $\tilde{\cdot}$  denotes the spatial filtering operator. Note that, in the following sections,  $\tilde{\cdot}$  denotes the coherent flow quantities. Furthermore,  $x_i$  denotes the coordinate in direction  $i$ ,  $\tilde{u}_i$  denotes the velocity,  $\tilde{p}$  denotes the pressure,  $\tilde{\theta}$  denotes the potential temperature,  $\nu$  denotes the molecular viscosity, and  $Pr$  denotes the Prandtl number. The subgrid stresses and heat flux terms are denoted by  $\tau_{ij} = \tilde{u}_i \tilde{u}_j - \tilde{u}_i \tilde{u}_j$  and  $\tau_{0j} = \theta \tilde{u}_j - \tilde{\theta} \tilde{u}_j$  and represent the interactions with the unresolved quantities. Their impact on the flow is modeled using the standard Smagorinsky model<sup>30</sup> with AMR-Winds default Smagorinsky constant of  $C_s = 0.135$ . The additional source term  $C_i$  represents the Coriolis forces,  $B_i$  represents the buoyancy term (both zero in this study), and  $F_i$  represents other force terms, including those introduced by the turbine via the actuator model. AMR-wind is the second-order accurate in time and space. This is achieved with a combination of finite-volume method and finite-element method for the spatial discretization and a Godunov method for the advection terms.<sup>28,31</sup>

The turbine is placed in a computational domain that covers a volume of  $19 \times 12 \times 12 D^3$  as schematically presented in Fig. 3. The turbine is centered in the lateral directions  $y$  and  $z$  with a distance of  $6D$  to the lateral boundaries and  $5D$  to the inlet. Based on previous works<sup>32–35</sup> and the grid convergence study presented in App. B, the wake region of  $0 < x/D < 10$  in streamwise direction and  $-2 < y/D < 2$  and  $-2 < z/D < 2$  in horizontal and vertical directions, is resolved with 80 cells per diameter (CpD), which corresponds to a cell size of  $\Delta x = \Delta y = \Delta z = 1.57$  m. This is achieved by successively nesting four grid refinements starting from the base grid with a resolution of 5 CpD. Each refinement is placed  $1D$  apart from the adjacent coarser refinement level and increases the grid resolution by a factor of two. This results in a computational grid with approximately  $162 \times 10^6$  cells throughout the domain. The inlet boundary condition at  $-5x/D$  is defined as mass inflow with a density of  $\rho = 1.225$  kg  $m^{-3}$ , and the outlet at  $14x/D$  as pressure outflow boundary condition. The side walls in both lateral directions are modeled as slip walls.

The turbine is modeled using the actuator line method (ALM) following the methodology presented by Sørensen *et al.*<sup>36</sup> The ALM models the blades as a distribution of discrete forces along rotating straight lines. The discrete forces are determined from the coupled wind turbine simulation tool OpenFAST, based on the lift and drag coefficient lookup

tables corresponding to the respective airfoils along the blade and the local relative velocity sampled from the LES grid at each actuator point. The blades are discretized with 55 points along the blade span. The discrete forces must be projected onto the surrounding points in the LES grid by means of a Gaussian regularization kernel to avoid numerical instabilities.<sup>33</sup> As highlighted by Martinez *et al.*,<sup>32</sup> the resulting wake is sensitive to the width of the Gaussian kernel  $\varepsilon$ . Ideally,  $\varepsilon$  equals the chord length of the blade profile at the blade tip, which is  $c = 1.419$  m at the investigated turbine. To ensure the correct projection of the force onto the numerical grid, it also must spread over at least two grid cells. Balancing these two aspects, we chose  $\varepsilon = 3.2$  m  $> 2\Delta x$ . The blades are assumed to be rigid. The helix approach is defined via the *Active Wake Control* feature, included in the ROSCO<sup>37</sup> turbine controller, coupled to the *ServoDyn* module. We investigate the wake of a helix with non-dimensional frequency  $St = 0.3$  and a pitch amplitude of  $\hat{\beta} = 3^\circ$  in CW and CCW direction. These helix setpoints are selected based on Taschner *et al.*<sup>12</sup> and van der Hoek *et al.*<sup>13</sup> to lay within the optimal  $St$  range and guarantee a sufficiently strong perturbation to trigger a pronounced reaction of the wake.

The time is discretized with a constant time step of  $\Delta t = 0.02$  s to satisfy the Courant-Friedrichs-Lewy condition at the blade tip of  $CFL_{tip} = (u_{tip} \Delta t) / \Delta x = 0.88 < 1$ , where the tip speed is estimated as  $u_{tip} \approx TSR \cdot u_\infty < 70$   $ms^{-1}$ . Each simulation is advanced for 500 seconds, corresponding to about 1.9 flow-through times of the free flow before data are acquired to ensure that the initial transient is excluded. Then, data are collected during ten helix periods  $T_e$ , where one period corresponds to  $T_e = 46.66$  s. During the first nine periods after the run-up phase, the flow is sampled in the region of the finest grid refinement with grid resolution at four equidistant phase instances per period. These data are then used for the triple decomposition described in Sec. II C 1. During the last period, the same domain is sampled with a sampling frequency of 10 Hz to obtain a time-resolved representation of the helix. The mean flow is calculated in an on-the-fly procedure over the last ten periods.

### C. Flow analysis

Generally, a wind turbine wake recovers by exchanging mean kinetic energy with the surrounding flow. The observed enhancement

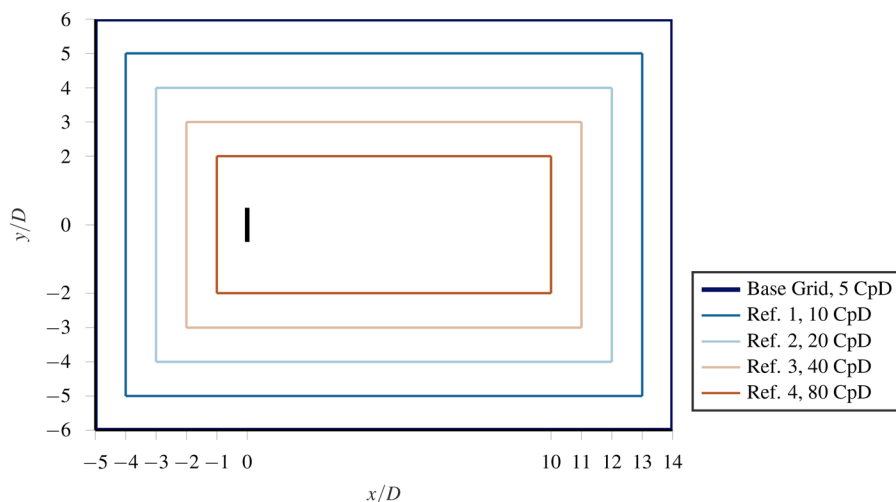


**FIG. 3.** Schematic representation of the LES domain. The back line represents the swept area of the turbine. The axis ticks indicate the domain extensions and the locations of the grid refinements. The resolution of the different grid regions is quantified by the number of cells per diameter (CpD).

in wake recovery with helix active wake control suggests that the mechanisms facilitating this energy exchange differ from those of conventionally controlled wind turbines. This section introduces various methods to investigate these mechanisms, seeking deeper insights into the underlying effects of helix wake control and the impact of the actuation-swirl alignment.

### 1. Triple decomposition

To investigate whether the helix enhances the energy exchange with the surrounding flow by accelerating the generation of random turbulence or by inducing coherent, periodic motions associated with the excitation frequency, the flow is decomposed into mean, random, and periodic velocity contributions using the triple decomposition as introduced by Hussain and Reynolds.<sup>38</sup> Accordingly, the  $i$ th component of the velocity  $u_i(t)$  at each point in the domain at time  $t$  consists of

$$u_i(t) = \bar{u}_i + \tilde{u}_i(t + nT_e) + u'_i(t), \quad (5)$$

where  $\bar{u}_i$  denotes the mean flow,  $\tilde{u}_i$  denotes the contribution of coherent, periodic fluctuations, and  $u'_i$  denotes the random fluctuations. Using Einstein's summation convention, the subscript  $i = 1, 2, 3$  denotes the three coordinate directions  $x$ ,  $y$ , and  $z$ . The number of the period is denoted by  $n$  and the excitation period of the helix  $T_e$ . The computation of  $\tilde{u}_i$  and  $u'_i$  requires phase-averaging the flow field at one phase instance  $\varphi$  over  $N$  samples as

$$\langle u_i(t) \rangle = \frac{1}{N} \sum_{n=0}^{N-1} u_i(t + nT_e). \quad (6)$$

Then, the coherent velocity components are obtained as

$$\tilde{u}_i(t) = \langle u_i(t) \rangle - \bar{u}_i, \quad (7)$$

and the random velocity components as

$$u'_i(t) = u_i(t) - \tilde{u}_i(t) - \bar{u}_i. \quad (8)$$

For the sake of readability, the remainder of this paper omits the explicit notation of the temporal dependency  $t$ . Having decomposed the flow into its mean, coherent, and random components, also their contributions to the kinetic energy  $\bar{K}$  can be computed as

$$\bar{K} = \bar{K}_M + \bar{K}_C + \bar{K}_R = \frac{1}{2} \bar{u}_i \bar{u}_i + \frac{1}{2} \overline{\tilde{u}_i \tilde{u}_i} + \frac{1}{2} \overline{u'_i u'_i}, \quad (9)$$

where  $\bar{K}_M$  denotes the kinetic energy of the mean flow,  $\bar{K}_C$  denotes the kinetic energy of the coherent fluctuation, and  $\bar{K}_R$  denotes the kinetic energy of the random fluctuations.

### 2. Fluxes of mean kinetic energy

To investigate the effect of  $\bar{K}_C$  and  $\bar{K}_R$  on the wake recovery, we quantify the associated transport of mean kinetic energy. Therefore, we define the wake area as the cylindrical volume  $V$  between the rotor tips of two aligned turbines as schematically presented in Fig. 4. The downstream turbine can only harvest energy from the streamwise mean kinetic energy contained within that volume. Consequently, increased transport of mean kinetic energy from the surrounding flow across the lateral boundary of the wake control volume  $S_{\text{cyl}}$  (rendered

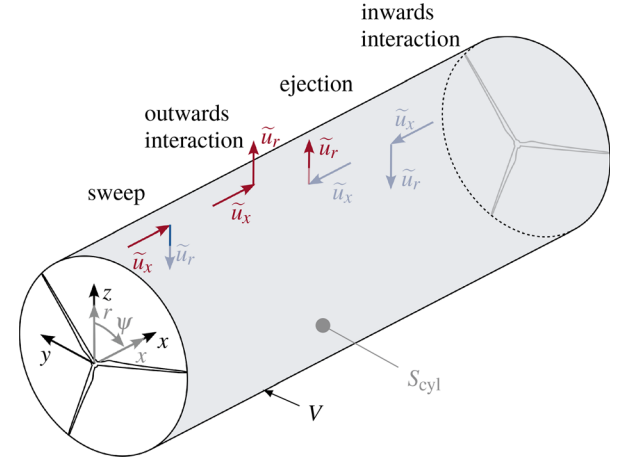


FIG. 4. Schematic of the four types of mean kinetic energy fluxes over the cylindrical surface  $S_{\text{cyl}}$  into the wake control volume  $V$ . Additionally, the orientation of the Cartesian coordinate system is indicated in black, and the cylindrical coordinate system in gray.

in gray color) into the wake enhances the kinetic energy available for the downstream turbine, allowing for increased power production of both turbines together.

To validate that, we analyze the transport equation of mean kinetic energy as derived by Reynolds & Hussain,<sup>39</sup> which is obtained by multiplying the momentum equation of the Navier–Stokes equations for inviscid flows and no body forces

$$\frac{\partial u_i}{\partial t} + u_j \frac{\partial u_i}{\partial x_j} = -\frac{1}{\rho} \frac{\partial p}{\partial x_i}, \quad (10)$$

where  $\rho$  denotes the density and  $p$  denotes the pressure, with the mean flow  $\bar{u}_i$ . Phase averaging yields the transport equation of kinetic energy for one phase  $\varphi_0$

$$\begin{aligned} (\bar{u}_j + \tilde{u}_j) \frac{\partial K_M}{\partial x_j} = & -\frac{1}{\rho} \left( \frac{\partial \bar{p}}{\partial x_i} + \frac{\partial \tilde{p}}{\partial x_i} \right) - \bar{u}_i \left( \frac{\partial \tilde{u}_i}{\partial t} + \tilde{u}_j \frac{\partial \tilde{u}_i}{\partial x_j} \right) \\ & - \left( -\langle u'_i u'_j \rangle - \tilde{u}_i \tilde{u}_j \right) \frac{\partial \bar{u}_i}{\partial x_j} \\ & - \frac{\partial}{\partial x_j} \left[ \bar{u}_i \langle u'_i u'_j \rangle + \bar{u}_i (\tilde{u}_i \tilde{u}_j) \right]. \end{aligned} \quad (11)$$

The left-hand side describes the net rate of change of the mean-flow kinetic energy, where a positive rate implies recovery of the wake deficit. The right-hand side represents the governing mechanisms, namely, the transport of mean kinetic energy due to pressure gradients in the first term. The transport due to random and periodic fluctuations is expressed in the last term, which contains the fluxes of mean kinetic energy in Cartesian coordinates  $\Phi_{\text{cart}}$

$$\begin{aligned} \tilde{\Phi}_{\text{cart}} &= -\bar{u}_i (\tilde{u}_i \tilde{u}_j), \\ \Phi'_{\text{cart}} &= -\bar{u}_i \langle u'_i u'_j \rangle. \end{aligned} \quad (12)$$

The second term describes the convection of mean kinetic energy with the mean flow, and the third term represents the reduction of mean



kinetic energy due to the creation of random and periodic fluctuations. Comparable analyses by Cal *et al.*<sup>40</sup> and Calaf *et al.*<sup>41</sup> revealed that the power generated by wind turbines in a wind farm is of the same order of magnitude as the transport of mean kinetic energy due to random and periodic fluctuations into the wind turbine region. Houtin-Mogrolle *et al.*<sup>42</sup> showed that the transport of mean kinetic energy also dominates the wake recovery of a single wind turbine. Consequently, we focus the analysis on the last term of Eq. (11), which describes the transport of mean kinetic energy due to random and coherent fluxes. Lignarolo *et al.*<sup>43</sup> applied a comparable methodology on PIV measurements at hub height of a greedily controlled wind turbine. Later, van der Hoek *et al.*<sup>17</sup> picked up that approach to analyze PIV measurements of a helix wake. Both works differ from the presented work in the frequency of the targeted coherent structures: while they focus on the tip-vortices with a periodicity of three times the rotor frequency, this work focuses on the structures related to the helix excitation frequency.

The effect of the transport fluxes on the mean kinetic energy available in the wake is obtained by integrating the last term of Eq. (11) over the cylindrical wake control volume  $V$  shown in Fig. 4. Applying Gauss's theorem, the volume integral transforms into a sum of surface integrals over the circular inlet, outlet, and cylindrical lateral surface  $S_{cyl}$ . The fluxes over the lateral surface  $S_{cyl}$  determine the additional amount of kinetic energy transported into the wake to be made available for the downstream turbine. This kinetic energy  $\mathcal{P}$  can be computed as

$$\mathcal{P} = \iint_{S_{cyl}} [\Phi'_{cart} + \tilde{\Phi}_{cart}] dS_{cyl}. \quad (13)$$

A larger  $\mathcal{P}$  indicates a higher wake recovery, making it a measure of the efficacy of the active wake control method.

The components of  $\Phi_{cart}$  with a radial component directed toward the wake center, or in other words perpendicular to  $S_{cyl}$ , have an integral effect on the wake recovery. To highlight these specific fluxes, we transform  $\Phi_{cart}$  from the Cartesian coordinate into the cylindrical coordinate system centered around the rotor center as visualized with gray arrows in Fig. 4. Therefore, we use the transformation matrix

$$\mathbf{T} = \begin{bmatrix} 0 & \cos \psi & \sin \psi \\ 0 & -\sin \psi & \cos \psi \\ 1 & 0 & 0 \end{bmatrix}, \quad (14)$$

where  $\psi = \tan^{-1}(-y/z)$  represents the azimuthal position aligned with the rotor's direction of rotation and the zero position at the rotor top. Then, the fluxes in the cylindrical coordinate systems are obtained as  $\Phi = \mathbf{T} \cdot \Phi_{cart} \cdot \mathbf{T}$ . Now, the components

$$\tilde{\Phi}_{xr} = -\bar{u}_x(\tilde{u}_x\tilde{u}_r) \quad \text{and} \quad \Phi'_{xr} = -\bar{u}_x\langle u'_x u'_r \rangle, \quad (15)$$

directly express the coherent and random transport of streamwise mean kinetic energy in the radial direction, being the relevant component for the wake recovery process.

### 3. Quadrant analysis

Wallace *et al.*<sup>44</sup> provide a physical interpretation of the fluxes by classifying the possible combinations of differently signed velocity fluctuations in Eq. (15) on the wake recovery through quadrant analysis.

For the sake of brevity, we present the following theory only by means of coherent components ( $\tilde{\cdot}$ ), but it equally applies to the random components ( $\cdot'$ ). Four combinations of signs may occur: two in which  $\tilde{u}_x$  and  $\tilde{u}_r$  are signed opposite and two in which they are signed equally. Figure 4 visualizes these combinations schematically, where the blue arrows represent a negative fluctuation and the red arrows a positive fluctuation. Equally signed combinations ( $\tilde{u}_x < 0$  and  $\tilde{u}_r < 0$ ; or  $\tilde{u}_x > 0$  and  $\tilde{u}_r > 0$ ) describe interactions where either low-momentum air is moved toward the wake center or high-momentum air away from the wake center. These fluxes result in a net negative transport of mean kinetic energy and, thus, decelerating the wake recovery. A negative fluctuation in streamwise direction  $\tilde{u}_x < 0$  combined with a positive fluctuation toward the wake center  $\tilde{u}_r > 0$  describes a process where low-momentum fluid is displaced outside the wake center, named ejection. The other opposite signed combination, where  $\tilde{u}_x > 0$  and  $\tilde{u}_r < 0$ , describes a sweep that moves high-momentum air toward the wake center. Ejection and sweep events result in a net positive mean kinetic energy transport into the wake; hence, they contribute to the wake recovery. This allows us to classify the fluxes of mean kinetic energy as  $\Phi_{xr,q}$  with

$$q = \begin{cases} \text{ejection,} & \text{if } \tilde{u}_x < 0 \text{ and } \tilde{u}_r > 0, \\ \text{sweep,} & \text{if } \tilde{u}_x > 0 \text{ and } \tilde{u}_r < 0, \\ \text{inward interaction,} & \text{if } \tilde{u}_x < 0 \text{ and } \tilde{u}_r < 0, \\ \text{outward interaction,} & \text{if } \tilde{u}_x > 0 \text{ and } \tilde{u}_r > 0. \end{cases} \quad (16)$$

For the sake of readability, only the initial letters, printed in bold, will be used to denote each flux type in the remainder of the paper. As such, the quadrant analysis yields further insights into the dominant wake recovery mechanisms triggered by helix active wake control.

## III. RESULTS

The presentation of the results in this section follows a causal order, starting with the thrust force perturbation that helix active wake control induces on the flow at the rotor plane, which represents the initial trigger for the phenomena in the wake in Sec. III A. This perturbation leads to significant deformations of the wake shape and its quantities, as shown in Sec. III B. The explanation for these deformations is given in Sec. III C by identifying and quantifying a system of coherent vortices. Section III D shows that these vortices actively transport mean kinetic energy into the wake and thereby accelerate the wake recovery.

### A. Thrust force perturbation at the rotor plane

We start by analyzing the response of the turbine to the pitch actuation induced by helix active wake control. Therefore, Table II

**TABLE II.** Change of temporal mean and standard deviation  $\sigma$  over ten helix periods to the baseline for effective wind speed at the rotor  $u_{eff,rotor}$ , rotor thrust  $F_{T,total}$  and aerodynamic power  $P_{aero}$ .

	CW		CCW	
	Mean rel. to BL	$\sigma$ rel. to BL	Mean rel. to BL	$\sigma$ rel. to BL
$u_{eff,rotor}$	+0.02%	+77.7%	+0.016%	+39.1%
$F_{T,total}$	-0.24%	+273.3%	-0.09%	+220.8%
$P_{aero}$	-0.82%	+789.3%	-1.22%	+474.8%

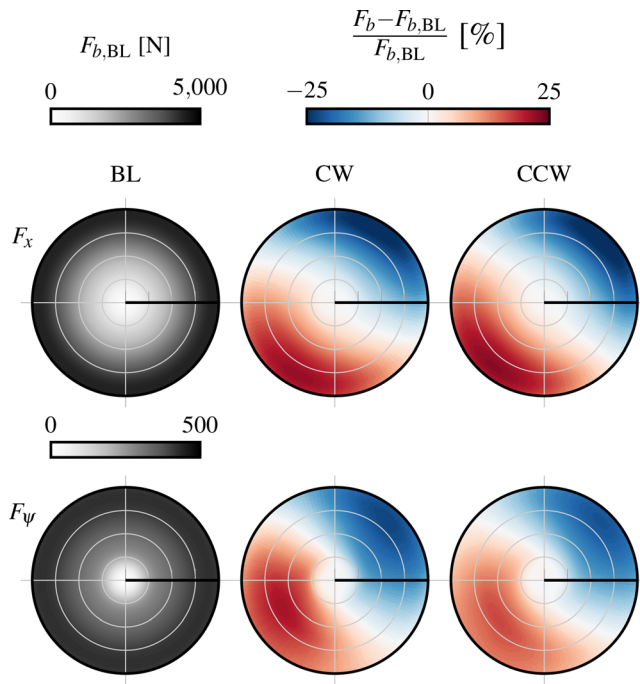


**FIG. 5.** Streamwise and azimuthal force distribution  $F_x$  and  $F_\psi$  over the rotor plane for the baseline case in the left panel, and the force perturbation  $\tilde{F}_{b,\text{Helix}}$  superimposed by the CW helix in the middle panel and the CCW helix in the right panel.

summarizes the temporal averages and standard deviations  $\sigma$  computed over ten helix periods of the effective wind speed at the rotor  $u_{\text{eff,rotor}}$  obtained by averaging the velocity over the rotor disk, the rotor thrust  $F_{T,\text{total}}$ , and the aerodynamic power  $P_{\text{aero}}$ .

As expected from previous studies, helix active wake control reduces the mean aerodynamic power generated by the actuated turbine. These losses come with a reduction of the total rotor thrust and an increase in the effective rotor wind speed. While all the investigated mean values experience only slight changes on the order of one percent compared to the baseline, the cyclic pitching of the blades leads to an order of magnitude higher increase in the standard deviation, which is more pronounced in the CW case than in the CCW case. This implies that standard momentum theory, which assumes steady flow regimes, cannot be applied to a turbine actuated with helix active wake control. Instead, it may be noted that trends such as the correlation of rotor thrust and aerodynamic power do not hold anymore, since the CW helix experiences a higher thrust force reduction but smaller power losses than the CCW helix. Therefore, we proceed with an analysis that accounts for the unsteadiness induced by the helix.

For this purpose, we first analyze the force field  $F_b(r, \psi)_{\varphi_0}$  that the flow experiences at the rotor plane in one phase instance  $\varphi_0$ . Given the uniform inflow and ground-free domain,  $F_b(r, \psi)$  only varies its azimuthal orientation over the entire helix excitation period but retains the shape from  $\varphi_0$ . At the  $i$ th phase instance  $\varphi_i$ , the helix force field has rotated by  $\psi_{\text{Helix},i}$ , and the blade itself has rotated by  $\psi_{\text{Blade},i}$  in the azimuthal direction. Note that  $\psi_{\text{Helix},i} \geq 0$  for the CW helix and  $\psi_{\text{Helix},i} \leq 0$  for the CCW helix. Now, the blade and the helix force field

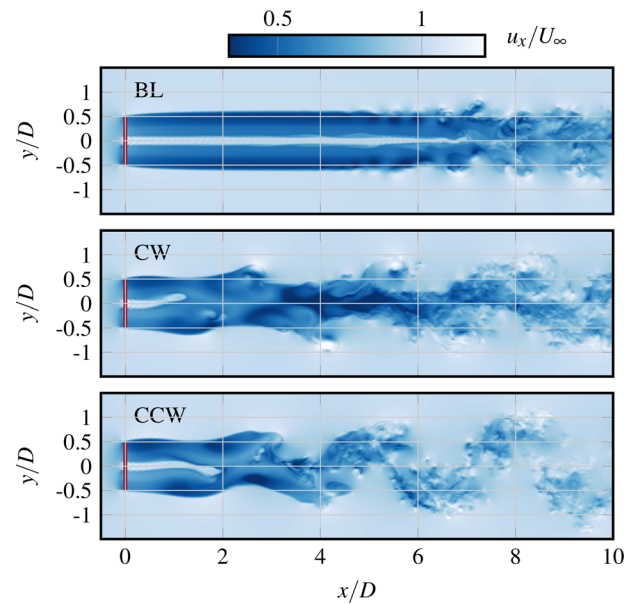


**FIG. 6.** Snapshots of the instantaneous streamwise velocity  $u_x$  at hub height. The red lines indicate the position of the rotor.

can be rotated by  $\psi_{\text{Helix},i}$  against the rotational direction of the helix to match  $\varphi_0$

$$\psi_{\text{Blade},0} = \psi_{\text{Blade},i} - \psi_{\text{Helix},i}. \quad (17)$$

Since the rotational frequencies of helix and rotor are different also  $\psi_{\text{Helix},i}$  and  $\psi_{\text{Blade},i}$  are unequal, hence also  $\psi_{\text{Blade},i}$  and  $\psi_{\text{Blade},0}$  differ. Thus, this approach successively fills up the entire rotor plane with the blade force profiles  $F_b(r)_{\varphi_i}$  rotated into  $\varphi_0$  to supply the distribution of  $F_b(r, \psi)_{\varphi_0}$  over the rotor plane. We found that  $i_{\text{max}} = 240$  phase instances suffice to cover the rotor plane sufficiently.

The left column of Fig. 5 presents the streamwise and azimuthal components, and  $F_x$  and  $F_\psi$  of the absolute  $F_{b,\text{BL}}(\psi, r)$  in the baseline case. As expected, both components are symmetrically distributed around the rotor center, with  $F_x$  being orders of magnitude larger than  $F_\psi$ .

The middle and the right panel visualize the perturbations  $\tilde{F}_{b,\text{Helix}}(\psi, t)$  CW and CCW helix active wake control superimposes on the baseline thrust obtained as  $\tilde{F}_{b,\text{Helix}} = F_{b,\text{Helix}} - F_{b,\text{BL}}$  at one phase instance as suggested by Eq. (1). Each component is normalized with its corresponding baseline distribution  $F_{b,\text{BL}}$ , which reveals that each component experiences a perturbation of up to around 25% compared to its baseline value. The shape of  $\tilde{F}_{b,\text{Helix}}$  is similar for CW and CCW helix: both force components increase on one rotor half plane and decrease on the other as a reaction to the pitch excitation. Thereby  $F_x$  concentrates in the outer 25% of the blade span, while  $F_\psi$  achieves its highest values between 50% and 75% of the radius. Over one helix period, these patterns perform one rotation around the rotor center, either in the CW or CCW direction.

In conclusion, the similarity of  $\tilde{F}_{b,\text{Helix}}$  for CW and CCW helix at the given phase instance shows that both perturb the flow equally strongly. The differences in the wake, presented in the following



sections, must consequently arise from the differing dynamics induced by the opposite rotational directions.

### B. Instantaneous and mean wake

To investigate the effect of the previously described helix force perturbation on the wake, Fig. 6 compares the instantaneous streamwise velocity field  $u_x$  at hub height between baseline, CW helix, and CCW helix.

The baseline wake exhibits the expected symmetric shape, featuring a stable wake until  $x/D \approx 5$ . In this region, a shear layer shields the wake from the surrounding flow, thereby preventing both regimes from mixing and recovering the wake velocity deficit. Beyond  $5D$ , a perturbation develops in the shear layer, which eventually causes it to break down and initiate the turbulent mixing of the wake and the surrounding flow. The missing inflow turbulence delays the onset of the wake breakdown compared to a wake in realistic atmospheric conditions. The wake breakdown point in laminar conditions is highly sensitive to the numerical setup, in particular, the grid size and the order of the numerical scheme together with the operational parameters of the turbine and the inflow conditions, but also the LES scheme in general.<sup>45</sup> Considering these aspects, the wake breakdown point matches well with the results from Trolborg *et al.*<sup>33</sup> and Cheung *et al.*<sup>25</sup> The high velocity region in the wake center corresponds to the hub jet which results from the lower energy extraction in the hub region compared to the blade tips.

The wakes generated by helix active wake control exhibit distinct characteristics. The non-uniform thrust perturbation unevenly decelerates the flow over the rotor plane, which translates to regions of enhanced and decreased velocity deficits in the near wake. These velocity perturbations first deform the hub jet and then periodically deflect the wake in the lateral direction. In the far wake, the deflected wake structure becomes increasingly turbulent. Even though that general shape holds for CW and CCW helix, they differ in the secondary

features in the wake. In the CW helix wake, predominantly exposed structures are displaced laterally, while the wake center remains centered around the rotor. In contrast, in the CCW helix, the entire wake is displaced in the lateral direction and disperses faster into turbulent structures. Thus, the alignment of the helix actuation with respect to the wake swirl activates distinct mechanisms, as evident in the different instantaneous wake shapes.

We proceed by investigating the impact of these distinct features on the mean flow, which finally governs the energy available to be harvested by a waked turbine. Therefore, Fig. 7 visualizes the streamwise mean flow component  $\bar{u}_x$  as a fraction of the free wind speed  $u_\infty$  at hub height for all the three investigated cases.

The trends observed in the instantaneous flow are also reflected in the mean flow fields. Both helix cases induce significant deformations in the mean wake structure compared to the baseline case. While the baseline wake remains stable until  $x/D \approx 5$ , the helix moves the onset of the wake recovery upstream. Moreover, CW and CCW helix generate distinct structures inside the wake. The CW helix shortens the hub jet more than the CCW helix but creates a concentrated mean kinetic energy deficit in the wake center between  $3.5 \lesssim x/D \lesssim 6$ . In contrast, the CCW helix primarily disperses the wake in the region of  $2 \lesssim x/D \lesssim 4$ , resulting in a more diffused wake further downstream. To further quantify the wake recovery, the right panel of Fig. 7 integrates over the area shadowed by the rotor  $S_{\text{rotor}}$  in the streamwise direction into the wake as

$$\mathcal{K}_{M,x} = \frac{1}{S_{\text{rotor}}} \iint_{S_{\text{rotor}}} \frac{K_{M,x}}{K_{M,\infty}} dS_{\text{rotor}}. \quad (18)$$

This serves as a measure of the kinetic energy available for a fully waked downstream turbine. In general, both helix cases move the onset of the wake recovery further upstream compared to the baseline in the investigated flow regimes. CW and CCW helix are congruent in the near wake area until they start diverging from  $x/D = 2$  onward.

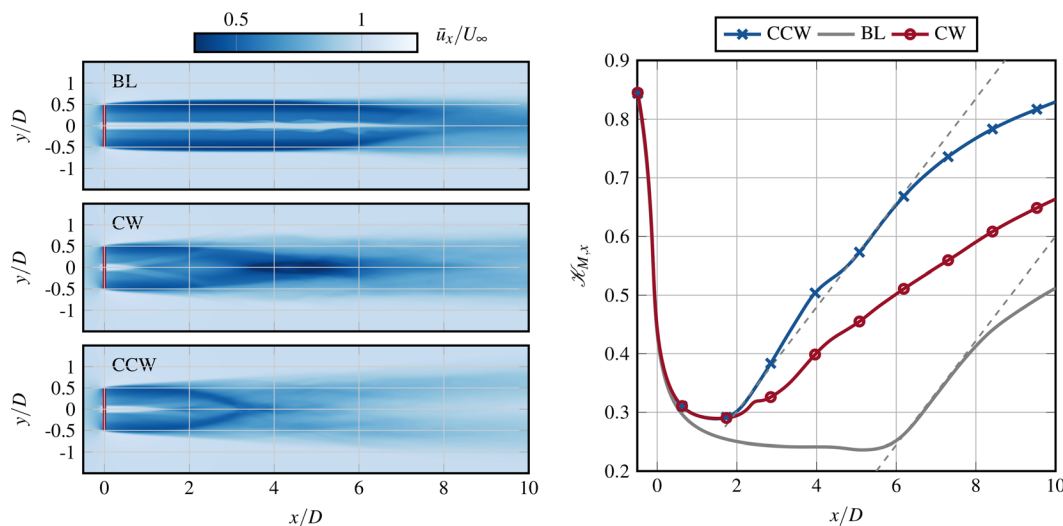


**FIG. 7.** Left panel shows the temporal average of the streamwise velocity  $\bar{u}_x$  normalized with the free wind speed at hub height for baseline, CW helix, and CCW helix. The red lines indicate the rotor position. The right panel integrates the mean kinetic energy over a circular surface of diameter  $D$  centered around the hub. This serves as a measure of the energy available to a fully waked downstream turbine. The gray dashed lines indicate the initial wake recovery rate of the baseline case.

This suggests that the mechanisms causing that divergence require a certain distance to establish. Then, the CCW helix wake constantly features higher levels of mean kinetic energy than the CW helix wake, which is consistent with previous studies.<sup>11,16,17</sup>

In addition to the absolute values of the available mean kinetic energy, the wake recovery rate, as indicated by the slope of  $\mathcal{K}_{M,x}$ , is of interest. The recovery rate of the baseline immediately after the onset of the wake recovery is represented by the gray dashed lines. It appears that the baseline wake only maintains its high initial recovery rate over the first  $2D$  before it diverges to lower rates. Even though the CW helix moves the onset of the wake recovery upstream, it never reaches the recovery rates of the baseline. In contrast, the CCW helix outperforms the recovery rates of the baseline directly after the wake recovery onset and maintains comparable levels until  $x/D = 6$  before it diverges to lower levels. Thus, CW and CCW helix not only accelerate the onset of the wake recovery but also impact the wake recovery rate.

In summary, helix active wake control manipulates the shape of the wake, the mean flow, and the available mean kinetic energy compared to the baseline case. Consistent with previous studies, the CCW helix accelerates the wake recovery more than the CW helix.

### C. Coherent vortex structures

To further understand the unequal deformation of the wake shape and the enhancement of the wake recovery between CW and CCW helix, observed in the previous section, we investigate the coherent vortex structures in the wake. For this purpose, we first identify the vortices using the  $Q$ -criterion and. Then, we quantify the radial vortex core position and the vortex strength in terms of the circulation  $\Gamma$ .

#### 1. Vortex identification

To identify the coherent vortex structures in wakes we use the normalized  $Q$ -criterion,<sup>46,47</sup> computed as

$$Q = \frac{u_\infty^2}{D^2} \frac{1}{2} (\Omega_{ij}\Omega_{ij} - S_{ij}S_{ij}) = -\frac{u_\infty^2}{D^2} \frac{1}{2} \frac{\partial u_i}{\partial u_j} \frac{\partial u_j}{\partial u_i} > 0, \quad (19)$$

where  $\Omega_{ij}$  denotes the symmetric and  $S_{ij}$  denotes the antisymmetric part of  $\nabla \mathbf{u}$ . The  $Q$ -criterion is a widely used method to identify and visualize vortices. In wind turbine research, it has mostly been applied to identify tip and hub vortices in wind tunnel experiments<sup>17,48</sup> and numerical simulations.<sup>49</sup>

Figure 8 visualizes the spatially coherent vortex structures in the wake at one time instance through isosurfaces of  $Q = 2 \times 10^{-4}$ . This value of  $Q$  has been tuned manually to represent the dominant vortex structures clearly. The isosurfaces are colored by the streamwise vorticity component  $\omega_x$  to indicate the rotational direction of the vortex. A vortex with  $\omega_x < 0$  (blue) rotates in the CCW direction, and a vortex with  $\omega_x > 0$  (red) rotates in the CW direction, viewing from upstream the turbine in the direction of the free flow.

The baseline wake shows the typical structures of a wind turbine wake. In the wake center resides the straight hub vortex rotating in CCW direction against the rotational direction of the rotor. Each blade tip sheds a tip vortex that propagates helically into the wake until it diffuses. Classic tip-vortex breakdown mechanisms such as vortex pairing and leapfrogging are not resolved due to the numerical diffusion of the applied second-order scheme on the chosen grid resolution and the

regularization of the ALM. The wake breakdown process initiates at  $x/D \approx 4$ , with the creation of larger vortices in the wake boundary. Due to the absence of ambient turbulence and turbulence-triggering components such as tower, nacelle, and ground, as well as the resolution of the spatial discretization, the onset of the wake breakdown is delayed compared to a turbine exposed to realistic atmospheric flow conditions.

The near rotor wake of both helix types features tip and hub vortices until  $x/D \approx 1.5$ . In this region, the hub vortex already experiences a helical distortion. Further downstream, both helix cases give rise to a coherent vortex of the dimension of the hub vortex that emerges in the shear layer of the wake. It follows the rotation of the respective helix type, adopting a helical shape. As it propagates downstream, secondary turbulent vortex structures establish around it that eventually dominate the wake.

To distinguish between features related to the helix excitation frequency and features living on turbulent random time scales, we perform a triple decomposition of the wake as described in Sec. II C 1. The classic triple decomposition requires averaging the flow field at one phase instance over  $N$  samples, where a higher  $N$  yields a higher convergence of the averaged quantity. To increase the number of samples, we exploit the point symmetry of the computational setup, where the phases only differ in their azimuthal orientation. Consequently, the number of samples  $N$  can be increased by averaging over four phase instances  $\pi/2$  apart after rotating each instance by  $\psi = \pm n\pi/2$  (+ for CW helix, − for CCW helix) around the domain center into the same phase. Accordingly, the phase-averaging procedure expressed in Eq. (6) adapts to

$$\langle u_i(t) \rangle = \frac{1}{N} \sum_{n=0}^{N-1} \mathbf{R}_x \left( \pm n \frac{\pi}{2} \right) u_i \left( t + n \frac{T_e}{4} \right), \quad (20)$$

where  $\mathbf{R}(\psi)$  is the rotational matrix around the streamwise oriented axis

$$\mathbf{R}_x(\psi) = \begin{bmatrix} 1 & 0 & 0 \\ 0 & \cos \psi & -\sin \psi \\ 0 & \sin \psi & \cos \psi \end{bmatrix}. \quad (21)$$

We apply that methodology over ten helix cycles, using four samples per cycle. Hence, the phase averages consider 40 samples. The remaining procedure of the triple decomposition remains the same as described in Sec. II C 1. The so-obtained phase averaged coherent structures related to the helix excitation Strouhal number of the helix are visualized in Fig. 9 in terms of the phase averaged  $Q$ -criterion  $\langle Q \rangle$ . Compared to the instantaneous structures shown in Fig. 8, the small-scale turbulent structures in the far wake are filtered out, revealing the full extension of the outer helical vortex. In both helix wakes, it extends until the end of the domain; however, in the CCW helix, the outer vortex appears more diffused toward the end of the domain than in the CW case.

Furthermore, the phase-averaging reveals the creation of smaller-scaled vortices related to the excitation  $St$  oriented opposite to the direction of rotation of the outer vortex. These structures establish at  $x/D \approx 3$  in the CCW helix and  $x/D \approx 4$  in the CW helix in the wake center and then bend around the outer vortex toward the wake boundary. Further downstream, these vortices decompose as they transition into random turbulence.

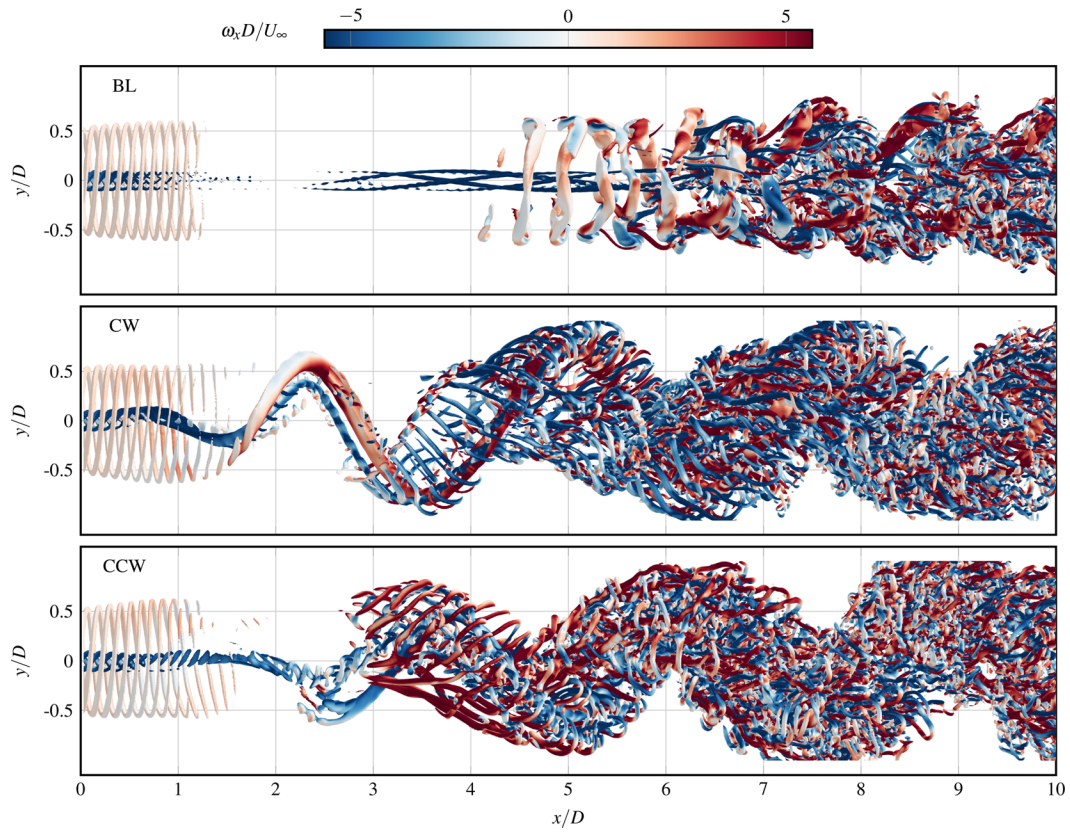


**FIG. 8.** Dominant vortex structures in instantaneous flow fields visualized as isosurfaces of the Q-criterion at  $Q = 2 \times 10^{-4}$ . The isosurfaces are colored by the streamwise vorticity component  $\omega_x$ , such that  $\omega_x > 0$  indicates a CW direction of rotation and a  $\omega_x < 0$  indicates a CCW direction of rotation.

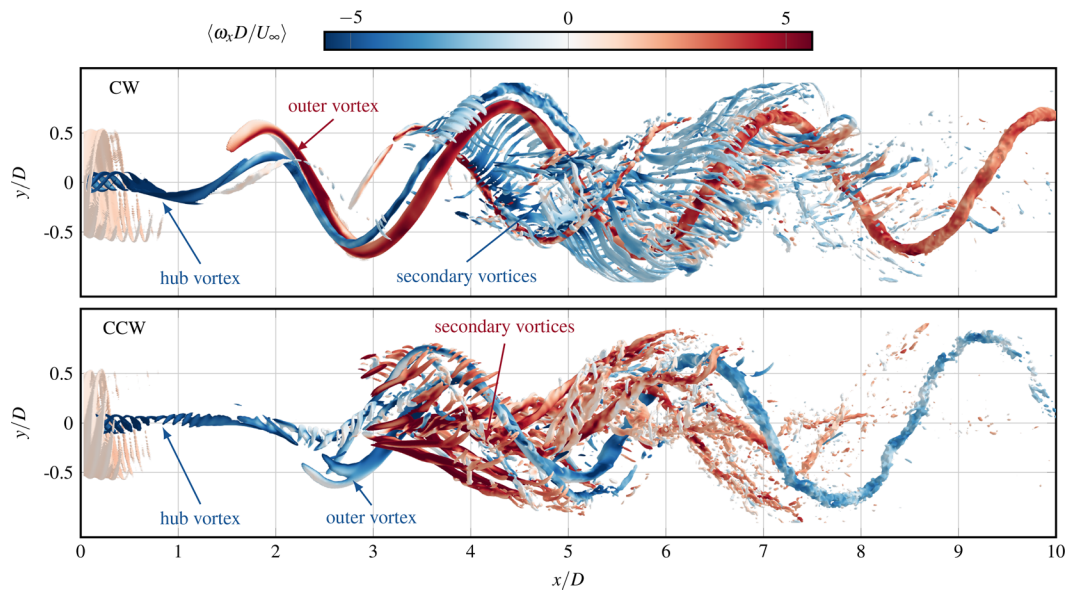


**FIG. 9.** Coherent vortex structures phase averaged at the excitation Strouhal number using isosurfaces of the Q-criterion at  $\langle Q \rangle = 2 \cdot 10^{-4}$ . The isosurfaces are colored by the streamwise vorticity component  $\langle \omega_x \rangle$ , such that  $\langle \omega_x \rangle > 0$  indicates a CW direction of rotation and a  $\langle \omega_x \rangle < 0$  indicates a CCW direction of rotation.



Although CW and CCW helix exhibit similar vortex features, they differ in certain characteristics. The first difference is the opposite direction of rotation of the outer vortex as indicated by the sign of  $\langle \omega_x \rangle$ . For the CW helix, the outer vortex rotates in CW direction, while it is in CCW direction for the CCW helix. In both wakes, the hub vortex rotates in the CCW direction. As a result, the outer vortex and hub vortex together form a system of co-rotating vortices in the CCW wake, whereas in the CW wake, it establishes a system of counter-rotating vortices in the near wake up to  $x/D \approx 3$  until the hub vortex dissipates. From other fluid dynamic phenomena co- and counter-rotating vortex pairs are known to feature distinct interaction dynamics. While co-rotating vortices tend to merge and form one large vortex, counter-rotating vortices rather interact in distinct instability patterns.<sup>50–55</sup> Even though, to the best of the author's knowledge, no comparable system of helical co- and counter-rotating vortices, as observed in this work, has ever been presented in the literature before, also in the helix wakes, the opposite aligned vortex pairs appear to reflect differing interaction mechanisms. Differences in the downstream wake evolution—such as the earlier formation of the outer vortex, delayed secondary vortex generation in the CW helix, accelerated outer vortex decay, and faster wake recovery in the CCW helix—may be influenced by the distinct vortex pairs in the near wake. The remainder of this paper focuses on the interaction of these vortices and their impact on the wake recovery.

## 2. Unwinding the coherent vortex structures

The intricate structure of the vortices presented in Figs. 8 and 9 makes it challenging to interpret their interaction mechanisms. This section facilitates their interpretation by unwinding the helix, as schematically represented in Fig. 10. In the global coordinate system, the outer vortex is helically shaped as presented in the previous section. The unwound coordinate system  $\mathcal{U}$  follows its helical shape by adapting its azimuthal orientation at each downstream position. Then, in the unwound coordinate system, the outer vortex appears as a straight-line vortex, allowing for the extraction of a two-dimensional plane that contains the outer vortex and the wake centerline.

On this plane, features aligned with the primary helical structure appear as large, coherent regions, while secondary-scale features manifest as recurring small-scale patterns.

Procedurally, the unwinding is achieved by first determining the position of the outer vortex core  $\mathbf{x}_{\text{vort, cart}} = (x, y, z)|_{\text{vort, cart}}$  with the algorithm described in Appendix A. Then,  $\mathbf{x}_{\text{vort, cart}}$  is transformed into a cylindrical coordinate system  $\mathcal{C}$  centered around the rotor center

$$\mathbf{x}_{\text{vort, } \mathcal{C}} = \begin{bmatrix} x \\ r \\ \psi \end{bmatrix}_{\text{vort, } \mathcal{C}} = \begin{bmatrix} x \\ \sqrt{y^2 + z^2} \\ \tan^{-1}\left(\frac{-y}{z}\right) \end{bmatrix}_{\text{vort, cart}}. \quad (22)$$

The same coordinate transform is used to transform any variable of interest described on the Cartesian computational grid into the cylindrical perspective. Now, we can unwind the helix by subtracting the azimuthal position of the outer vortex core  $\psi_{\text{vort, } \mathcal{C}}$  from the azimuthal coordinate vector

$$\mathbf{x}_{\mathcal{U}} = \begin{bmatrix} x \\ r \\ \psi \end{bmatrix}_{\mathcal{U}} = \begin{bmatrix} x \\ r \\ \psi - \psi_{\text{vort}} \end{bmatrix}_{\mathcal{C}}. \quad (23)$$

This approach applies equally to CW and CCW helix and potentially also to varying excitation frequencies without specific adaptations. However, it is susceptible to the accuracy of the vortex core identification.

Following this approach, the outer vortex is, by definition, located at the origin of the azimuthal coordinate of the unwound coordinate system  $\psi_{\mathcal{U}} = 0$ . Figure 11 shows the streamwise vorticity component  $\omega_x$  on that plane through the hub vortex core. Note that the dominant direction of the flow is no longer normal or parallel to that unwound slice.

In the unwound slice, the outer vortex appears as a continuous region of positive  $\omega_x$  (red) in the CW helix and as negative  $\omega_x$  (blue) in the CCW helix. Within that region, the black dashed line indicates the position of the vortex core, as obtained from the vortex tracing algorithm described in Appendix A.

As visible in the near wake region, up to  $x/D \approx 1$ , the outer vortex of the CW helix emerges directly from the natural wake shear layer

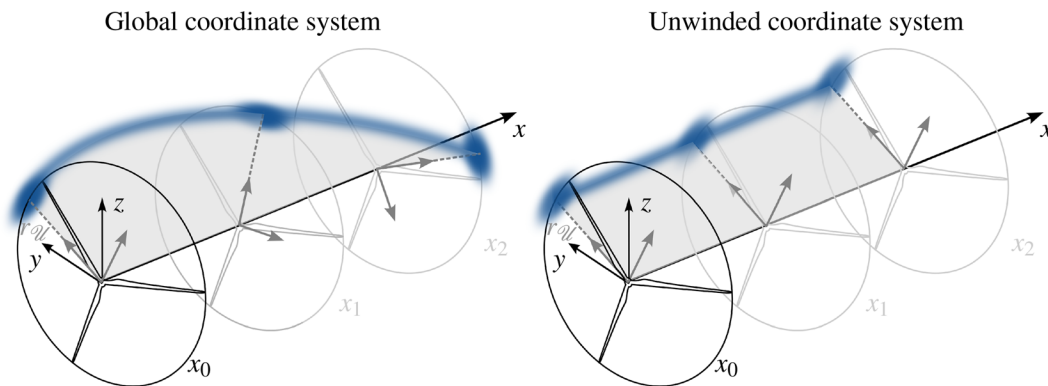


**FIG. 10.** Schematic representation of the unwinding process for the CCW helix. The global coordinate system is visualized in black, and the unwound coordinate system  $\mathcal{U}$  in gray at three exemplary downstream positions  $x_i$ . The blue area indicates the outer vortex. The gray surface represents the plane that contains the outer vortex and the wake center, which is plotted in Fig. 11.

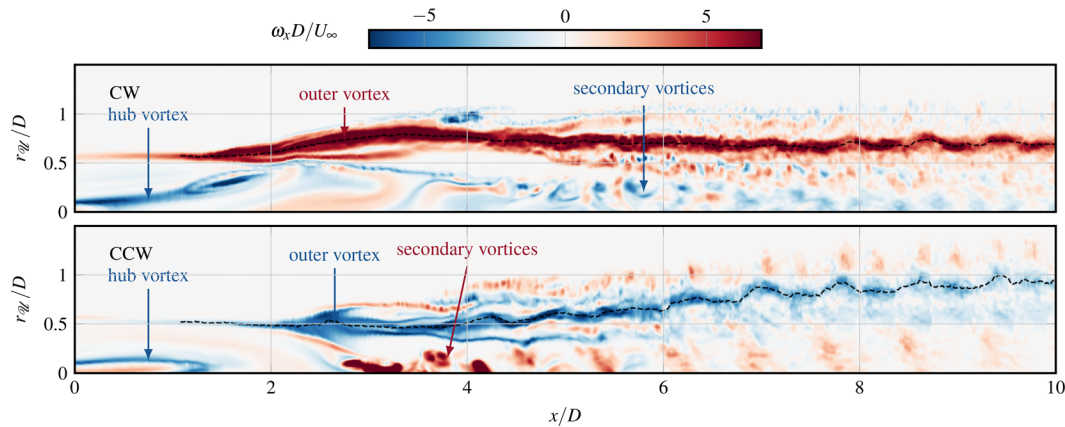


**FIG. 11.** Unwound slice through the outer vortex showing the streamwise vorticity  $\omega_x$ . The helix is unwound by rotating the outer vortex core at each streamwise position around the wake center into one plane. The outer vortex appears as a continuous region of positive or negative  $\omega_x$ . The black dashed line indicates the position of the outer vortex core.

marked by positive  $\omega_x$ . The shear layer gets strengthened and thickens up to grow into the outer vortex. On its further trajectory throughout the wake, it first increases its radial displacement away from the wake center to reach its maximum displacement between  $x/D = 3$  and 4. Then, it contracts again to maintain a constant distance to the wake center from  $x/D \approx 6$  onward. Thereby, it maintains its coherence throughout the wake. In contrast, in the CCW helix case, the shear layer vorticity first switches signs to negative  $\omega_x$ , which then gives rise to the outer vortex. Also, the trajectory of the CCW helix outer vortex throughout the wake differs from the CW helix. After its creation, it first contracts toward the wake center, reaching its minimal distance to the wake center at  $x/D \approx 3.5$ . From that point onward, it decays into turbulent structures, while increasing its radial position until the end of the domain.

The decay process of the outer vortex itself is, in both helix cases, characterized by the creation of secondary instabilities on the side facing the free flow. These satellite vortex structures are oriented opposite to the rotational direction of the outer vortex and have already been observed in Fig. 9. They appear weaker and smaller in the CW helix than in the CCW helix.

Of similar interest are the dynamics induced in the wake center. In the near wake region, the hub vortex experiences distinct types of distortions in CW and CCW helix. In the CW helix, it is displaced in lateral direction away from the wake center toward the outer vortex, as also visible in the isosurfaces shown in Figs. 8 and 9. Then, it rolls out of the visualized unwound plane around the outer vortex to intersect with it again at  $x/D = 4$ . In contrast, in the CCW helix, the hub vortex remains straight in the wake center before it decays at  $x/D \approx 1.5$ .

After the decay of the hub vortex, turbulent structures are generated in the wake center. In both cases, these structures rotate opposite to the outer vortex, forming a counter-rotating vortex pair as it has been observed by Coquelet *et al.*<sup>16</sup> and Korb *et al.*<sup>20</sup> Despite their presence in both helix cases, they differ in structure and intensity. In the CCW helix, they appear as detached coherent patches of positive  $\omega_x$  that develop shortly after the decay of the hub vortex at  $x/D \approx 3$ . Their initial intensity gradually disperses into larger, weaker structures as they propagate downstream. Thereby, they maintain a periodic

spacing between each other. In the CW helix wake, the turbulent patterns in the wake center are created further downstream than in the CCW helix at  $x/D \approx 6$ . Compared to the CCW helix, the center vorticity appears less intense and smaller.

In essence, the unwinding procedure showcases the discrepancies between the vortex systems in CW and CCW helix. Beyond opposite rotational direction, the outer vortex follows a distinct trajectory and decays faster in the CCW helix than in the CW helix. In both cases, vorticity oriented opposite to the outer vortex is created in both helix wakes, forming a counter-rotating vortex pair, but in the CCW helix, this center vorticity emerges further upstream.

### 3. Circulation of vortex system

Having described the vortex dynamics generated by helix active wake control in the previous Sections, we proceed with a quantitative analysis. For this purpose, we compute the streamwise circulation as a measure of the vortex strength of the outer vortex  $\Gamma_{x,\text{outer}}$  and the wake center vorticity  $\Gamma_{x,\text{inner}}$ . The circulation  $\Gamma_x$  is obtained by integrating vorticity  $\omega_x$  over a surface  $S_C$  that encloses the vortex and is oriented perpendicular to the vortex core. Thus, the streamwise circulation can be computed as

$$\Gamma_x = \iint_{S_C} \omega_x dS_C, \quad (24)$$

with  $S_C$  being a surface on a  $yz$ -plane. To measure  $\Gamma_{x,\text{outer}}$  and  $\Gamma_{x,\text{inner}}$ , we define two control surfaces  $S_{C,\text{outer}}$  and  $S_{C,\text{inner}}$ , such that they contain the respective vortex structures. Both surfaces are schematically visualized in the left panel of Fig. 12.

We use a circular surface centered around the hub with diameter of  $0.76, D$  as the control surface for the inner vortex  $S_{C,\text{inner}}$ . The smaller diameter than the rotor diameter is to ensure that  $S_{C,\text{outer}}$  and  $S_{C,\text{inner}}$  do not overlap. While  $S_{C,\text{inner}}$  is equal at each streamwise location in the wake, the control surface for the outer vortex  $S_{C,\text{outer}}$  follows the outer vortex as it circulates around the wake center. To accomplish this, we first identify the vortex core using the tracing algorithm described in Appendix A. Then,  $S_{C,\text{outer}}$  is defined at each streamwise

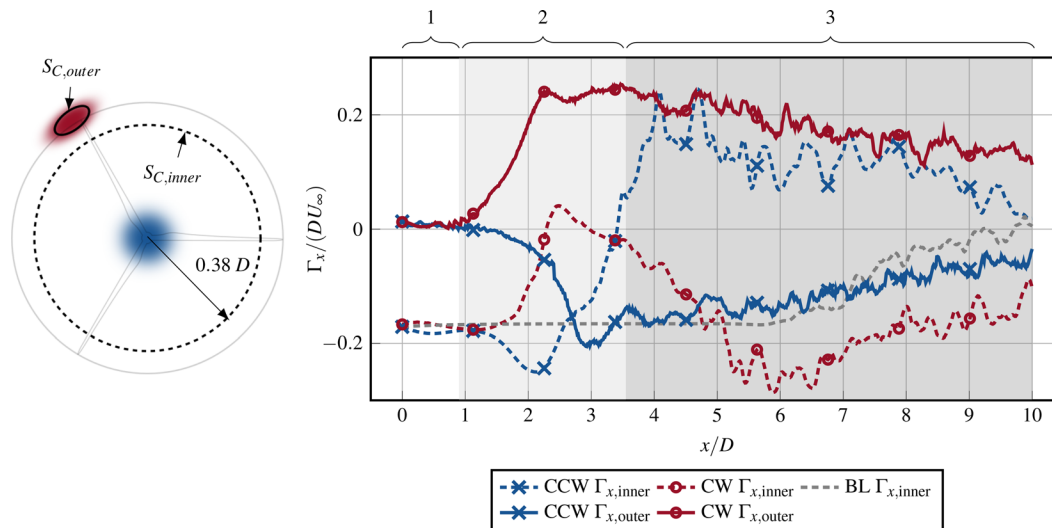


**FIG. 12.** Schematic visualization of the control surfaces  $S_{C,outer}$  (solid line) and  $S_{C,inner}$  (dashed line) used to compute the circulation of the vortices in the wake center  $\Gamma_{x,inner}$  and of the outer vortex  $\Gamma_{x,outer}$  in the left panel. The right panel quantitatively compares the vortex systems of CW and CCW helix using  $\Gamma_{x,inner}$  and  $\Gamma_{x,outer}$ . The waved brackets indicate the subdivision of the wake into three streamwise sections: (1) near wake perturbation, (2) generation of the vortex pairs, and (3) decay of the outer vortex.

position as the area encircled by the Q-criterion isoline of  $Q = 2 \cdot 10^{-4}$  around the vortex core. The so-obtained circulations of the inner and outer vortex between CW and CCW helix are compared in the right panel of Fig. 12. The wake center circulation of the baseline indicates the strength of the hub vortex and serves as a reference to compare the helix cases.

Both helix wakes exhibit comparable evolutions of the vortex circulation through the wake, which suggests a subdivision into three sections as indicated by the waved brackets above the plot. In region 1, from  $0 < x/D < 1$ , the force perturbation induced at the rotor plane is recognizable in the flow as a velocity perturbation. In the second region 2, from  $1 < x/D < 3.4$ , the near wake perturbation triggers the growth of the outer vortex, which then forms together with the hub vortex a co-rotating vortex pair in the CCW helix and a counter-rotating vortex pair in the CW helix. The last region 3, from  $3.4 < x/D < 10$ , contains the creation and decay of vorticity oriented opposite to the outer vortex in the wake center to form a counter-rotating vortex pair in both wakes. A detailed description of each section is given hereafter.

*a. Region 1: Near wake perturbation.* The low levels of  $\Gamma_{x,outer}$  imply that the outer vortex has not yet developed. However,  $\Gamma_{x,inner}$  reflects the force perturbation induced at the rotor plane, as indicated by the deviations from the baseline  $\Gamma_{x,inner}$ . The CW helix enhances the negative circulation of the hub vortex and the CCW helix decreases it. The crossflow slices at  $x/D = 0.35$  given in Fig. 13 highlight the differences of these perturbations.

Note that the color bar limits have been adjusted to enhance the visibility of the weaker wake center structures, which makes the hub vortex and shear layer appear oversaturated. The velocity field of the baseline wake is symmetrically distributed around the wake center, with the hub jet in the wake center and a pronounced velocity deficit around it. As indicated by the white quiver plot, the wake features a swirling motion in CCW direction. This velocity field translates to a

vorticity field that features the hub vortex in the wake center and the wake shear layer characterized by positive  $\omega_x$  at the wake boundary.

Both helix types disturb the point symmetric velocity field observed in the baseline by increasing the velocity deficit on one side of the wake and decreasing it on the other side. Interestingly, the CW helix reduces the CW-oriented swirl motion in the enhanced wake deficit region, whereas the CCW helix increases it in that region. Thus, the impact of the alignment of the helix actuation with the wake swirl may already be noted within a short distance behind the rotor. These differences are also recognizable in the vorticity fields. In contrast to the baseline, both helix types create a lobe of positive vorticity within the rotor plane, which appears more concentrated in the CW helix than in the CCW helix. This also affects the wake shear layer, which decreases its thickness close to that generated positive vorticity spot. On the other side of the rotor, the swirl motion is enhanced compared to the baseline case, notable by the regions of negative vorticity.

*b. Region 2: Generation of vortex pairs.* The second region is characterized by the generation of the outer vortex and the creation of oppositely oriented vorticity in the wake center. As visible in Fig. 12, the circulation of the outer vortex  $\Gamma_{x,outer}$  grows for both helix cases in opposite directions until it saturates. This process initiates further upstream in the CW helix than the CCW helix, potentially due to the CW helix outer vortex profiting from the equally signed vorticity in the shear layer. In contrast, the CCW helix outer vortex must first invert the shear layer vorticity, which also causes the CW helix outer vortex to reach its peak intensity further upstream at  $x/D \approx 2.2$  than the CCW helix, which saturates at  $x/D \approx 3$ . In absolute values, the outer vortex of the CW helix peaks at a stronger circulation than the outer vortex of the CCW helix.

Simultaneously with the growth of the outer vortex, the hub vortex decays in both helix types, as indicated by the decrease in the negative center circulation  $\Gamma_{x,inner}$  toward zero. Again, this process initializes further upstream in the CW helix than in the CCW helix.



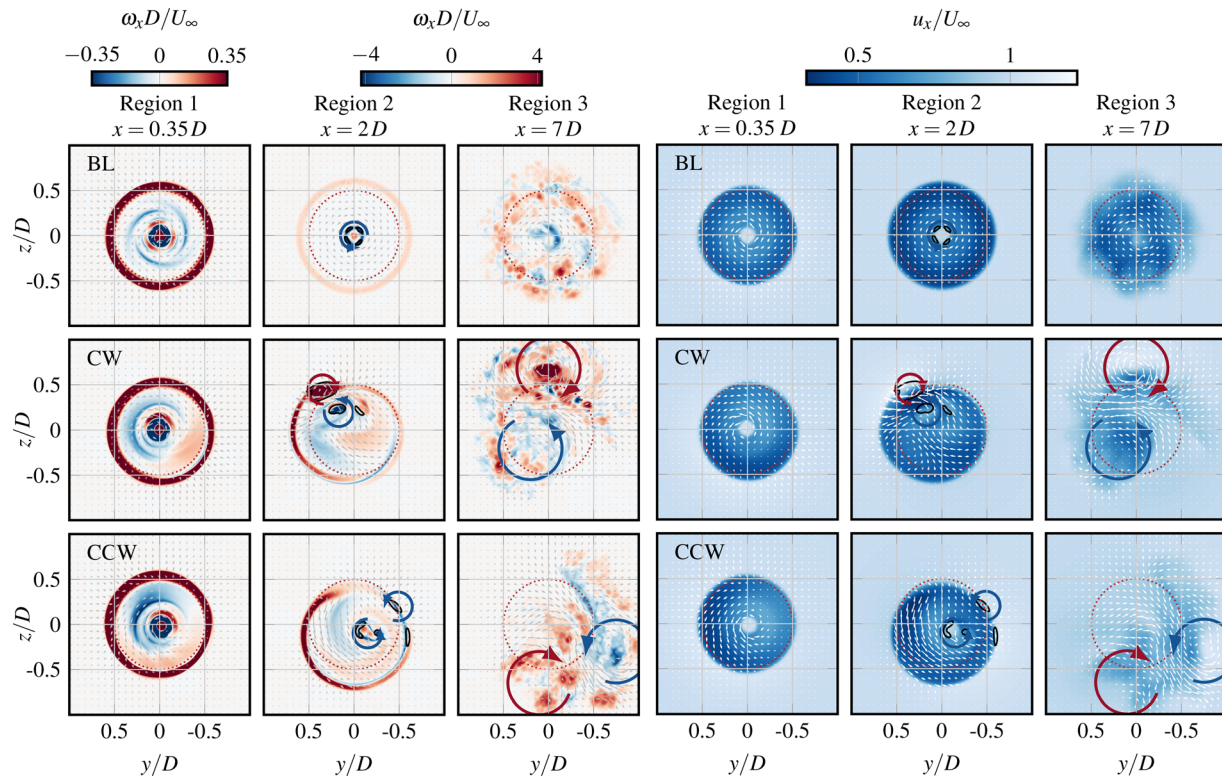


**FIG. 13.** Crossflow slices of streamwise vorticity  $\omega_x$  in the left panel and streamwise velocity  $u_x$  in the right panel. Each slice corresponds to one of the three sections indicated in Fig. 12. The circular arrows indicate the rotational direction of dominant vortex structures, where blue represents a CCW rotation, and red represents a CW rotation. Additionally, the black contour lines plotted in the  $x = 2D$  slices represent  $Q = 2 \times 10^{-4}$  to highlight the position of the vortex pair. The quiver plots indicate motions in the crossflow direction. The red dashed line indicates the rotor-swept area.

Before its decay, the hub vortex forms together with the outer vortex a co-rotating vortex pair in the CCW helix as indicated by  $\Gamma_{x,inner}$  and  $\Gamma_{x,outer}$  being equally signed. In contrast, in the CW helix,  $\Gamma_{x,inner}$  and  $\Gamma_{x,outer}$  are signed opposite, indicating a counter-rotating vortex system. These distinct vortex pairs have already been observed in Figs. 8 and 9.

The effect of the co-rotating or, respectively, counter-rotating vortex systems on the near wake, is highlighted in the  $u_x$  and  $\omega_x$  crossflow slices at  $x/D = 2$  in Fig. 13. The position of the vortices is indicated by the black contour lines of  $Q = 2 \cdot 10^{-4}$ , which is the same iso-value as shown in Fig. 8. In addition to the sign of  $\omega_x$  inside the  $Q$ -contourlines, red and blue arrows indicate the rotational direction of the vortices to enhance the comprehensiveness of the vortex systems. The quiver plot indicates the induced crossflow motions. The baseline wake is still plot symmetrically distributed around the center.

The  $\omega_x$  slices reveal that both helix types locally enhance the shear layer on one side and reduce it up to a sign flip on the other side. In the CW helix, the outer vortex emerges in the enhanced shear layer with a CW rotation direction. In contrast, in the CCW helix wake, the outer vortex is generated in the reduced shear layer, resulting in its rotation in CCW direction.

These distinct vortex pairs cause different dynamics in the wake. In the CW helix, the velocities induced between hub vortex and the outer vortex align, intensifying the crossflow motions in that region. In

contrast, the velocities induced between the co-rotating vortices in the CCW helix are oriented against each other. They counteract and the crossflow motions in that intermediate region remain low. However, the motions on the opposite side of the hub vortex are enhanced compared to the baseline. The induced crossflow motions cause both helix wakes to shift in the lateral direction, as evidenced by the position of the velocity deficit relative to the rotor area.

*c. Region 3: Counter-rotating vortices in far wake.* After the decay of the hub vortex at the end of region 2, at the beginning of region 3  $\Gamma_{x,inner}$  returns to grow into a new peak signed opposite to  $\Gamma_{x,outer}$ , implying the creation of the counter-rotating vortex pair that has already been observed in Sec. III C 2. This process includes a switch of sign of the center circulation of the CCW helix. Compared to the CW helix,  $\Gamma_{x,inner}$  of the CCW helix grows faster and peaks further upstream. In the remainder of region 3, the counter-rotating vortex system decays as implied by  $\Gamma_{x,inner}$  and  $\Gamma_{x,outer}$  trending toward zero. At the end of the domain, the vortex pair of the CW helix has higher levels of circulation than the CCW helix.

Both vortex pairs are identifiable as diffuse regions of positive and negative vorticity in the  $\omega_x$ -crossflow slices at  $x = 7D$  shown in Fig. 13. The blue and red arrows highlight their position and direction of rotation. As apparent in the crossflow slices of  $u_x$ , the crossflow motions are governed by the presence of the two counter-rotating

vorticity fields. Similar to the counter-rotating vortices in region 2 of the CW helix, the two counter-rotating vortices induce equally oriented velocities between them, generating motions in crossflow direction in their intermediate region in both helix types. This pushes the wake radially away from the wake center, deforming the wake into a kidney shape. The same phenomena were observed by Coquelet *et al.*<sup>16</sup> and Korb *et al.*<sup>20</sup> in LES of helix wakes. Comparable counter-rotating vortices, generating a kidney-shaped wake, are also known to be the driver for the lateral displacement of the wake of yaw-misaligned turbines.<sup>21,56,57</sup> In contrast to the static vortex pair in the yaw-misaligned wake, the vortex pair in the helix wake rotates around the wake center following the rotation of the helix force perturbation. Consequently, the displaced wake also rotates around the wake center at a constant radial position, giving it its name-giving helical shape.

In conclusion, Fig. 12 gives an overview of the phenomena described in the previous sections, beginning with the near wake perturbation in region 1, followed by the development of the outer vortex in region 2. The initially asymmetric configurations—comprising a counter-rotating vortex system in the CW helix and a co-rotating vortex system in the CCW helix—evolve into counter-rotating vorticity structures in region 3.

Furthermore, the observations presented in Sec. III C convey several indications for the interaction modes of the co- and counter-rotating vortex pairs in region 2. As already mentioned previously, co-rotating pairs of straight line vortices are known to merge into one vortex, while counter-rotating pairs break down following instability patterns.<sup>50–55</sup> Despite the additional complexity added by the helical outer vortex, several parallels to the well-known line vortices can be identified, as for instance the crossflow motions induced by the vortex pairs at  $x/D = 2$ , represented by the quivers in Fig. 13. Similar to a pair of counter-rotating line vortices, the counter-rotating vortex pair in the CW helix induces strong crossflow motions between them. In the case of line vortices, these induced motions result at a later stage in a cooperative elliptic instability.<sup>55</sup> Vice versa, the crossflow motions between the two co-rotating vortices in the CCW helix wake cancel out, as known from the early stages of the merging process of co-rotating line vortices.<sup>53</sup> Further implication is given by the radial position of the outer vortex visible in the unwound slices in Fig. 11. In the CW helix, the outer vortex is first pushed away from the wake center, followed by the hub vortex, which suggests mutual interactions of both vortex structures. Instead, the outer vortex of the CCW helix gets pulled toward the wake center, indicating a merging with the hub vortex. The interaction of both vortices in the CW helix is visible in Fig. 9, where the hub vortex follows the shape of the outer vortex until  $x/D \approx 5$ , whereas in the CCW helix the hub vortex already dissolves between  $x/D = 2$  and  $x/D = 3$ . Despite these implications for the interaction mechanisms of the co- and counter-rotating vortices, an in-depth study focusing exclusively on the helical configuration of two vortices is still required to explain the vortex interaction modes fully.

#### D. Impact of coherent vortices on fluxes of mean kinetic energy

Having described and quantified the vortex dynamics generated by CW and CCW helix in the wake, we now investigate their effect on the wake recovery process. For this purpose, we quantify the fluxes of mean kinetic energy induced by the coherent vortices and their effect on the mean kinetic energy contained in the wake.

#### 1. Kinetic energy in coherent and random structures

We first compare the kinetic energy contained in coherent structures  $K_C$  to the kinetic energy in random fluctuations  $K_R$  obtained with Eq. (9) using the triple decomposition described in Sec. II C 1. Both components are normalized with the free stream mean kinetic energy  $K_{M,\infty} = \frac{1}{2} u_\infty u_\infty$  and integrated in the lateral direction as

$$\mathcal{K}_C = \frac{1}{D^2} \int_{-1.5D}^{1.5D} \int_{-1.5D}^{1.5D} \frac{K_C}{K_{M,\infty}} dy dz, \quad (25a)$$

$$\mathcal{K}_R = \frac{1}{D^2} \int_{-1.5D}^{1.5D} \int_{-1.5D}^{1.5D} \frac{K_R}{K_{M,\infty}} dy dz. \quad (25b)$$

Note that in contrast to Eq. (18), we now integrate over the entire crossflow plane from  $-1.5D$  till  $1.5D$  in both lateral directions instead of only the area shadowed by the rotor. This is to capture the entire wake and not only the part that affects an aligned turbine.

The so-obtained distributions of  $\mathcal{K}_C$  and  $\mathcal{K}_R$  throughout the wake are compared in Fig. 14 for both helix cases with the baseline. In the baseline, the kinetic energy is exclusively contained in the random fluctuations, which are established from  $x/D \approx 4$  onward. The coherent kinetic energy associated with the helix excitation frequency remains negligible due to the absence of a corresponding periodic forcing. Thus, the baseline reflects the transition from a laminar to a turbulent wake by generating turbulent kinetic energy at random timescales and timescales that differ from those of the helix actuation. Helix active wake control changes the distribution of kinetic energy between coherent and random structures. For CW and CCW helix, the random kinetic energy establishes further upstream than in the baseline at  $x/D \approx 3$  but remains below the baseline throughout the rest of the domain. In contrast, the kinetic energy in coherent structures is enhanced throughout the wake. From the rotor plane onward, it steeply increases until it peaks at  $x/D \approx 3$ , orders of magnitude higher than the baseline or the random kinetic energy in the helix cases. The CCW helix reaches higher levels than the CW helix before both steadily decrease throughout the rest of the domain. The periodic spikes overlaying that decay are due to a lateral displacement of the wake beyond the integration bounds.

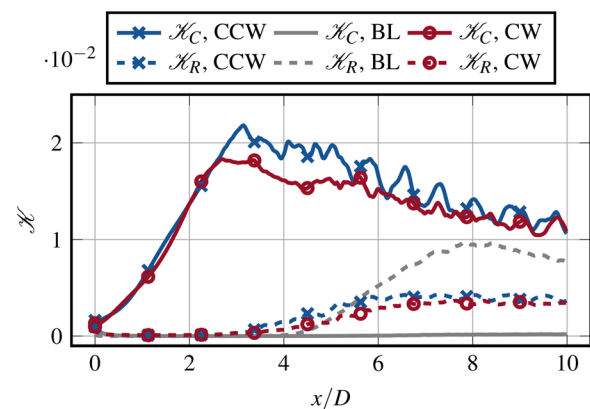
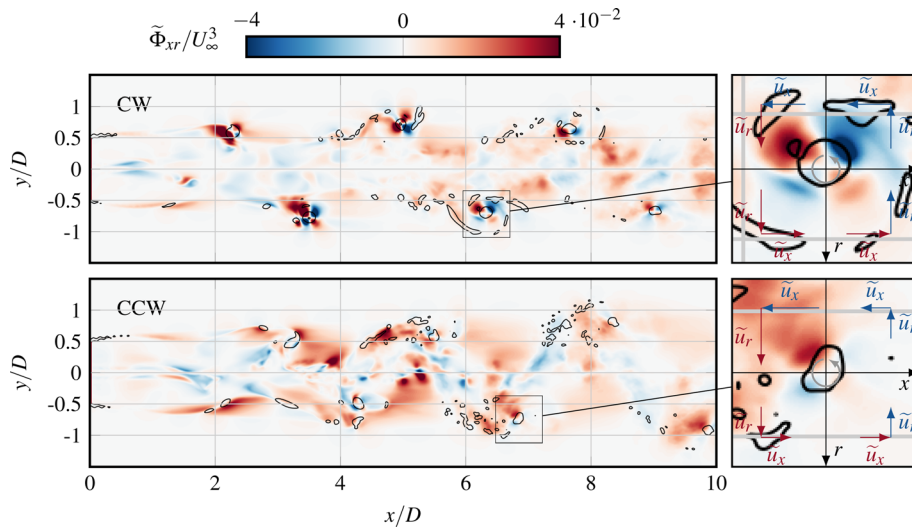


FIG. 14. Total kinetic energy contained in coherent structures  $\mathcal{K}_C$  and in random fluctuation  $\mathcal{K}_R$  throughout the streamwise extension of the wake.



**FIG. 15.** Fluxes of coherent mean kinetic energy directed toward the wake center  $\tilde{\Phi}_{xr}$  at hub height. A positive value is oriented toward the wake center, representing a contribution to the re-energization of the wake. The black iso-contours represent  $\langle Q \rangle_{\text{filtered}} = 1.3 \times 10^{-3}$  to visualize coherent vortex structures. For clarity, the Q-criterion iso-contours are only plotted in the wake boundary for  $\sqrt{y^2 + z^2} \geq 0.4D$ . Within the zooms into the fluxes around one vortex, the gray arrow indicates the direction of rotation of the vortex. The straight arrows indicate the orientation of the coherent fluctuations  $\tilde{u}_x$  and  $\tilde{u}_r$  additionally highlighted by the color (red indicates  $\tilde{u}_i > 0$ , blue indicates  $\tilde{u}_i < 0$ ).

Conclusively, Fig. 14 implies that in the laminar inflow conditions, the kinetic energy contained in the coherent vortex structures surpasses the kinetic energy contained in the random turbulence developing around them. This suggests that these coherent structures also have a higher impact on the wake recovery than turbulent fluctuations. Consequently, the following sections will focus on the influence of coherent structures on the wake recovery.

## 2. Coherent fluxes of mean kinetic energy

To study the effect of the coherent structures on the wake recovery, we investigate the associated fluxes of mean kinetic energy, as introduced in Sec. II C 2. Figure 15 visualizes the coherent mean kinetic energy fluxes in radial direction  $\tilde{\Phi}_{xr}$  at hub height as obtained from Eq. (15). Positive fluxes are oriented toward the wake center, contributing to the wake recovery. Additionally, isocontours of the phase-averaged and spatially smoothened  $\langle Q \rangle_{\text{filtered}} = 1.3 \times 10^{-3}$  indicate the position of coherent vortex structures in the wake. To focus on the fluxes and associated dynamics at the wake boundary, contours are not plotted in the wake center for  $r \leq 0.4D$ .

In both helix cases, the fluxes  $\tilde{\Phi}_{xr}$  are located in the vicinity of the coherent vortices. However, the patterns differ between CW and CCW helix. In the CCW helix,  $\tilde{\Phi}_{xr}$  is more diffusely distributed over a larger area, whereas in the CW helix, it remains concentrated around the vortices. In both cases,  $\tilde{\Phi}_{xr}$  exhibits a characteristic quadrupole structure in the vicinity of the coherent vortices, as highlighted in the zooms into the relevant region. The quadrupole structure is particularly pronounced in the CW wake, whereas in the CCW wake, it appears weaker and less distinct from the turbulent structures around it.

The blue and red arrows in the zooms in Fig. 15 indicate the orientation of the periodic velocity fluctuations  $\tilde{u}_x$  and  $\tilde{u}_r$  induced around the vortex and considered for the computation of  $\tilde{\Phi}_{xr}$  as outlined in Eq. (15). Note that the zoomed vortices reside on the lower half of the hub height plane ( $y < 0$ ); thus, the positive direction of the  $r$ -axis points downward away from the wake center. On the upper half of the plane, the positive  $r$ -axis is oriented upward;

hence, the pattern around the vortices is mirrored along the  $x$ -axis. Blue arrows indicate a negative fluctuation and red arrows indicate a positive fluctuation.

Based on the different combinations of signs, the fluxes can in each quadrant be classified using the quadrant analysis described in Sec. II C 3. This reveals that each quadrant relates to a different type of flux. Starting in the upper left quadrant of the zoom, following the counterclockwise rotation of the vortex, the fluxes can be classified as an ejection  $\tilde{\Phi}_{xr,e}$ , followed by an outward-directed interaction  $\tilde{\Phi}_{xr,o}$ , a sweep  $\tilde{\Phi}_{xr,s}$ , and an inward-directed interaction  $\tilde{\Phi}_{xr,i}$ . In the CW helix, ejection and inward-oriented interaction appear stronger than the sweep and outward-oriented interaction. This relative trend holds for each vortex in the CW wake, however, with varying absolute strengths. On the contrary, in the CCW helix, the ejection is significantly enhanced compared to the other three events around the highlighted vortex.

Comparable quadrupole structures were observed by Lignarolo *et al.*<sup>43</sup> around the tip vortices in a wind turbine wake and similarly explained with the different signs of the velocity fluctuations  $\tilde{u}_x$  and  $\tilde{u}_r$  around a vortex.

In short, the distinct vortex systems in the CW and CCW helix wakes distribute the fluxes of mean kinetic energy differently throughout the wake. The CW helix generates concentrated quadrupole structures around the outer vortex, while the CCW helix distributes them over larger regions throughout the wake.

## 3. Coherent contributions to wake recovery

As shown in Fig. 15, CW and CCW helix distribute the mean kinetic energy fluxes differently throughout the wake. However, only those fluxes that transport mean kinetic energy across the wake boundary into the wake affect the wake recovery. To examine the contribution of each flux type  $\tilde{\Phi}_{xr,q}$  to the wake recovery, we integrate  $\tilde{\Phi}_{xr,q}$  over the lateral surface  $S_{\text{cyl}}$  of the cylindrical wake control volume shown in Fig. 4 as described in Sec. II C 2.

Figure 16 visualizes the fluxes of mean kinetic energy over  $S_{\text{cyl}}$  into the wake at one phase instance. Additionally, Fig. 16 specifies the



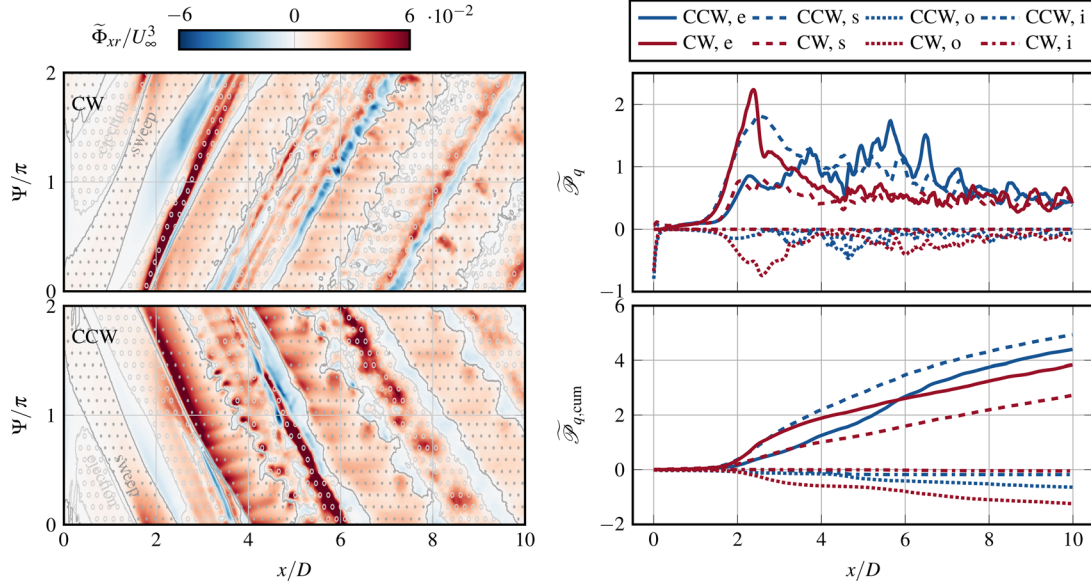


**FIG. 16.** Left panel visualizes the fluxes of mean kinetic energy  $\tilde{\Phi}_{xr}$  over the lateral surface of the wake control volume  $S_{Cyl}$  defined in Fig. 4 into the wake at one phase instance. The azimuthal positions  $\psi = 0\pi = 2\pi$  are defined as aligned with the vertical direction pointing upward. Additionally, sweeps are marked with  $\cdot$ , and ejections with  $\circ$ . The right panel integrates each type of mean kinetic energy fluxes over the azimuth  $\mathcal{P}_q$  in the upper panel and cumulates in streamwise direction  $\mathcal{P}_{q,cum}$  in the lower panel. The types of mean kinetic energy flux  $q$  are ejection, sweep, outward oriented interaction or inward oriented interaction. The bold letters represent the abbreviation used in the legend.

regions where sweep or ejection events trigger the positive fluxes of mean kinetic energy.

In both helix wakes, the fluxes of mean kinetic energy over  $S_{Cyl}$  into the wake are concentrated along diagonal structures. These structures reflect the helical shape of the wake, such that the direction of rotation of the helix explains the opposite-oriented inclinations of the structures. In the CW helix, the re-energizing fluxes are concentrated in coherent regions, whereas in the CCW helix they are more dispersed over larger areas. These regions follow the same recurring pattern throughout the wake in both helix types: along the streamwise direction, an ejection is followed by an interaction, then a sweep, and again an interaction. Further downstream, the boundaries between the regions, as well as the internal structures, become increasingly turbulent.

Even though the overall pattern is the same for CW and CCW helix, they differ in the details. First, the re-energizing fluxes are more intense and cover a larger region in the CCW helix than in the CW helix. Vice versa, the regions of negative fluxes that separate sweeps and ejections are less dominant and compact in the CCW helix. Second, the highest intensities are achieved by the ejections in the CW helix but by the sweeps in the CCW helix. Furthermore, the transition into turbulently blurred regions establishes further upstream such that the regions are incoherently scattered in the far wake.

To quantify the effect of each of the four types of fluxes on wake recovery, the right panel of Fig. 16 integrates  $\tilde{\Phi}_{xr,q}$  individually over the azimuth  $\psi$  at  $r = D/2$

$$\tilde{\mathcal{P}}_q(x) = \frac{1}{u_\infty^3} \int_0^{2\pi} \tilde{\Phi}_{xr,q}(r, \psi, x) r d\psi, \quad (26)$$

in the upper panel. The lower panel additionally cumulates them in streamwise direction as

$$\tilde{\mathcal{P}}_{q,cum}(x) = \frac{1}{Du_\infty^3} \int_0^x \int_0^{2\pi} \tilde{\Phi}_{xr,q}(r, \psi, x) r d\psi dx, \quad (27)$$

as a measure for the total coherent mean kinetic energy transported by each flux type into the wake up to a certain streamwise position.

Both helix types take up to  $x/D \approx 1.5$  until mean kinetic energy starts being transported into the wake. Then, the highest peak is achieved by the ejection in the CW helix and the sweep for the CCW helix, both between  $x/D = 2$  and  $x/D = 3$ . Thereby, the ejection in the CW wake reaches higher levels than the sweeps in the CCW helix. Further downstream, the ejections, being the second-strongest flux type of the CCW helix, gain dominant levels between  $5 < x/D < 6$ , while the second-strongest fluxes of the CW helix (sweeps) remain low. Furthermore, the outward-oriented interactions, which have negative effects on the wake recovery, peak in the CW helix between  $x/D = 2$  and  $x/D = 3$ . On the contrary, the CCW helix does not feature significant peaks of the inward- or outward-oriented interactions throughout the wake.

The peak transport of mean kinetic energy occurs in region 2 following the subdivision of the helix wakes introduced in Sec. III C 3. This region is characterized by the formation of the outer vortex, suggesting that the co- and counter-rotating vortex pairs in the CCW and CW helix, respectively, cause a major part of the mean kinetic energy transport into the wake, serving as a kick-start for the wake recovery.

Those trends are also reflected in the cumulated fluxes in the lower right panel of Fig. 16. The CCW helix experiences the strongest re-energization due to the sweeps, and the CW helix due to ejections. At  $x/D = 6$  the ejections of the CCW helix even overtake the ejections of the CW helix. The sweeps of the CW helix represent the smallest contribution to the wake recovery. In both helix cases, the outward-oriented interaction dominates the negative impacts on the wake

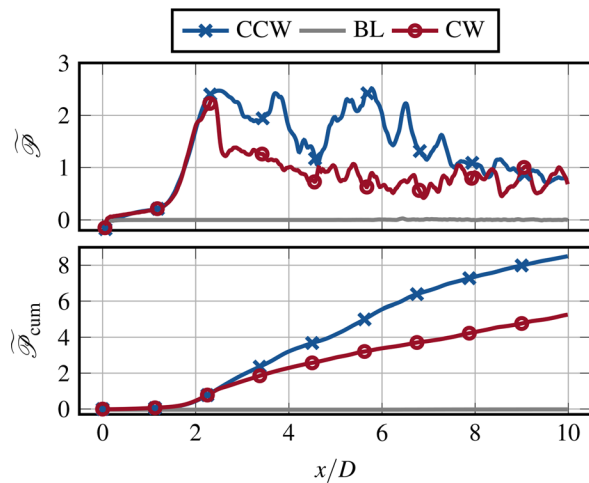


**FIG. 17.** Total mean kinetic energy transported over the cylindrical control surface  $S_{cyl}$  into the wake. The upper panel only integrates over the azimuth; the lower panel cumulates in a streamwise direction to quantify the additional energy available for a fully waked turbine.

recovery, which is stronger in the CW wake than in the CCW wake. The inward-oriented interactions remain on negligible levels throughout the domain. These observations confirm that the wake recovery enhancements generated by CW and CCW helix are caused by distinct vortex interaction principles. Namely, the counter-rotating vortex pair in the CW helix primarily enhances the mean kinetic energy in the wake by displacing lower energetic flow out of the wake region, whereas the co-rotating vortex pair of the CCW helix transports high energetic flow from the surrounding flow into the wake.

The total effect of all the types of mean kinetic energy fluxes together is obtained by summing over all of them

$$\tilde{\mathcal{P}}(x) = \sum \tilde{\mathcal{P}}_q(x), \quad (28a)$$

$$\tilde{\mathcal{P}}_{cum}(x) = \sum \tilde{\mathcal{P}}_{q,cum}(x), \quad (28b)$$

as a measure for the total additional mean kinetic energy made available for a fully waked turbine by helix active wake control.

The upper panel of Fig. 17 reveals that the intense sweep and ejection in the CCW helix, combined with low levels of negative fluxes, result in a larger amount of mean kinetic energy being transported into the wake than in the CW wake between  $x/D = 2$  and  $x/D = 8$ . The high peak of ejections in the CW wake observed in Fig. 16 is balanced by the negative impact of the outward-oriented interaction. As expected, the baseline shows no relevant fluxes related to the helix excitation frequency.

Cumulating  $\tilde{\mathcal{P}}$  in streamwise direction as shown in the lower panel of Fig. 17, indicates that from  $x/D \approx 3$  onward the mean kinetic energy transported by the coherent vortices of the CCW helix surpasses that of the CW helix. In other words, a fully waked turbine could harvest energy from a more energetic inflow when the upstream turbine applies the CCW helix instead of the CW helix. For instance, up to  $x/D = 5$ , a distance is used in many studies as the spacing between two aligned turbines, the CCW helix has transported 44.8 % more kinetic energy into the wake than the CW helix in the

investigated laminar conditions. Thus, the fluxes of mean kinetic energy induced by coherent vortex structures contribute to the differing efficacy of CCW and CW helix observed in Sec. III B and in previous studies.<sup>11,16–18</sup> A comparison with Fig. 12 further suggests that the wake recovery is governed primarily by the vortex structure rather than the circulation strength. This is evidenced by the outer vortex of the CW helix, which, despite exhibiting stronger circulation, contributes less mean kinetic energy to the wake.

#### IV. DISCUSSION

The findings presented previously complement the general understanding of the wake recovery mechanisms triggered by helix active wake control. Accordingly, the overall driver is the excitation of an unstable mode in the wake of the force perturbation at the rotor, as stated by Cheung *et al.*<sup>25</sup> The coherent vortices identified in this paper may be understood as a manifestation of that instability, which additionally explains the difference between CW and CCW helix. The tip vortices may interact with the coherent vortex structures, potentially affecting the tip vortex pairing as observed by van der Hoek *et al.*<sup>17</sup> or Mühle *et al.*<sup>18</sup> The relevance of the tip vortex manipulation for the overall wake recovery, compared to the energy entrained by the coherent structures throughout the extension of the wake, may be subject to future studies.

Future work may focus on the effect of more realistic inflow conditions on the coherent vortex structures. In a realistic boundary layer flow, including turbulence, veer, and shear, it is anticipated that the influence of coherent vortices on wake recovery decreases, and turbulent mixing processes gain relevance. The increased inflow complexity may reduce the spatial coherence of the vortex systems, accelerate their decay, and distort their shape, making their identification increasingly challenging. Nevertheless, their induced dynamics are still expected to impact the wake. Supporting that assumption, the phase-resolvable entrainment patterns created by coherent structures have already been identified in realistic offshore inflow conditions.<sup>22</sup> Furthermore, the counter-rotating vortices in the far wake,<sup>16,20</sup> and the differences between CW and CCW helix have already been observed in turbulent inflow<sup>16–18</sup> and in more realistic boundary layer flows.<sup>11</sup> Turbulence, veer, and shear likely influence the vortex dynamics and, consequently, the wake recovery differently. Understanding these effects could help identify optimal flow conditions for applying helix active wake control. Furthermore, the effect of different excitation Strouhal numbers is of similar interest.

The complemented understanding of the helix supplied in this paper might serve to reassess more advanced helix application scenarios. For instance, Korb *et al.*<sup>20</sup> and van Vondelen *et al.*<sup>58</sup> observe additional power gains when the downstream turbines synchronize their helix with an optimal phase alignment to the incoming helix of an upstream turbine. Another example is the combination of helix with dynamic yaw motions, as investigated by van den Berg *et al.*<sup>59</sup> and Gutknecht *et al.*<sup>60</sup> Both observe a strong dependency of the synergistic effects of both strategies on the phase alignment between helix and yaw motion. The reason for these phase dependencies has not yet been identified in both application cases. It is likely that the orientation of the vortex systems relates to the favorable phase alignments and could, therefore, contribute to their understanding and further optimization.

Apart from its phenomenological value, the coherent vortices give a promising ansatz for a physics-based helix wake model in the fashion of the curled wake model, presented by Martínez-Tossas

*et al.*<sup>61</sup> This model leverages the counter-rotating vortices behind a yaw-misaligned turbine to model the laterally displaced wake. Differently from the helix wake, in the yawed wake, the counter-rotating vortices remain statically at the wake top and bottom, displacing the wake only in the lateral direction. Obviously, a helix model would have to consider the rotation of the helix vortices, but the similarities between yaw-misaligned wake and helix wake observed in Sec. III C 3 promise the feasibility of a comparable model.

## V. CONCLUSIONS

This work analyzes the wake recovery mechanisms induced by helix active wake control. The key findings are, first, that helix active wake control generates a system of coherent vortices in the wind turbine wake that actively transports mean kinetic energy from the free flow into the wake and thereby contributes to the wake recovery. Second, the properties of these vortices differ between clockwise (CW) and counterclockwise (CCW) helix due to the opposite alignment of the helix actuation with the wake swirl. Finally, the vortex system generated in the CCW helix entrains a larger amount of mean kinetic energy into the wake, which contributes to the better performance of the CCW helix compared to the CW helix observed in previous studies.

## ACKNOWLEDGMENTS

This work is part of the Hollandse Kust Noord wind farm innovation program where CrossWind C.V., Shell, GROW, Eneco, and Siemens Gamesa are teaming up; funding for the PhDs was provided by CrossWind C.V. and Siemens Gamesa. The authors further acknowledge the computing resources provided by DelftBlue and thank SURF for the computational time made available on the Dutch national supercomputer Snellius (Grant No. EINF-10855).

## AUTHOR DECLARATIONS

### Conflict of Interest

The authors have no conflicts to disclose.

### Author Contributions

**J. Gutknecht:** Conceptualization (lead); Data curation (lead); Formal analysis (lead); Investigation (lead); Methodology (lead); Visualization (lead); Writing – original draft (lead); Writing – review & editing (lead). **E. Taschner:** Conceptualization (supporting); Data curation (supporting); Formal analysis (supporting); Investigation (supporting); Methodology (supporting); Validation (supporting); Visualization (supporting); Writing – review & editing (equal). **M. Coquelet:** Conceptualization (supporting); Data curation (supporting); Formal analysis (supporting); Investigation (supporting); Methodology (supporting); Validation (supporting); Visualization (supporting); Writing – review & editing (equal). **A. Viré:** Conceptualization (supporting); Formal analysis (supporting); Investigation (supporting); Methodology (supporting); Supervision (equal); Visualization (supporting); Writing – review & editing (equal). **J. W. van Wingerden:** Conceptualization (supporting); Funding acquisition (lead); Investigation (supporting); Methodology (supporting); Project administration (lead); Resources (lead); Supervision (lead); Validation

(supporting); Visualization (supporting); Writing – review & editing (supporting).

## DATA AVAILABILITY

The data that support the findings of this study are available from the corresponding author upon reasonable request.

## APPENDIX A: VORTEX TRACING ALGORITHM

The vortex core of the helical outer vortex is traced using the following algorithm.

**Require:** three-dimensional fields of  $Q$

```

1: Exclude Hub Vortex:
2: Set values within  $r < 0.4D$  to NaN
3: Initialize output array:
4:  $outerVortexPos \leftarrow$  zero arrays
5: create  $circularKernel$ 
6:  $xIdx \leftarrow 0$ 
7: for each  $crossflowPlane$  in  $Q$  field do
8:   convolute  $crossflowPlane$  with  $circularKernel$ 
9:   if  $xIdx == 0$  then
10:    Identify vortex core as maximum of  $Q$ :
11:     $outerVortexPos[xIdx] \leftarrow \max(crossflowPlane)$ 
12:   else
13:    search vortex core around previous vortex core location:
14:    Define circular search region with radius  $r_{search} = 0.1D$ 
    around  $outerVortexPos[xIdx - 1]$ 
15:    Mask  $crossflowPlane$  outside search region with NaN
16:     $outerVortexPos[xIdx] \leftarrow \max(crossflowPlane)$ 
17:   end if
18:    $xIdx \leftarrow xIdx + 1$ 
19: end for
20: return  $outerVortexPos$ 

```

## APPENDIX B: GRID CONVERGENCE STUDY

A grid convergence study has been conducted based on simulations with resolutions of 25, 50, and 80 CpD. Figure 18 presents the mean kinetic energy in the wake area shadowed by the rotor  $\mathcal{K}_{M,x}$  according to Eq. (18) obtained with the three different resolutions.

The following considerations imply that the resolution of 80 CpD sufficiently resolves the relevant phenomena in the flow for this study.

- (1) *Onset point of wake recovery of helix cases constant for different resolutions:* In the helix cases, the point where the near wake breaks down and the wake recovery initiates is located at  $x = 2D$  for all the investigated resolutions. As shown in Figs. 8, 9, 12, and 16, this is where the outer vortex achieves a relevant strength to initiate the transport of mean kinetic energy into the



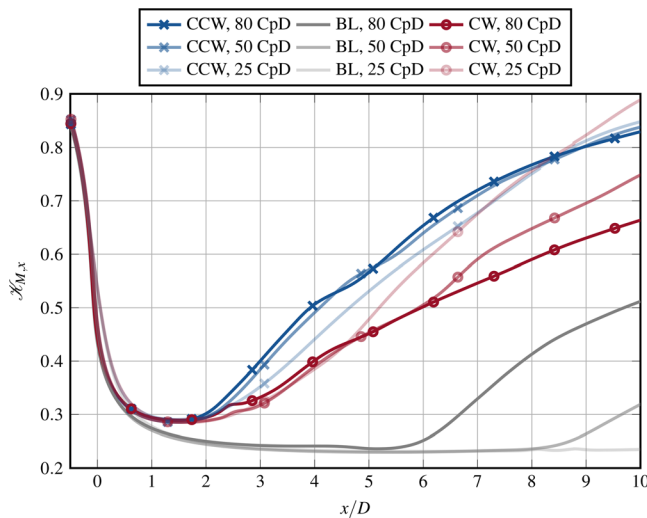


**FIG. 18.** Grid convergence study based on the mean kinetic energy in the wake  $K_{M,x}$  for grid resolutions of 25, 50, and 80 CpD.

wake and kick-start its transition. The fact that this point does not move with higher resolution implies that the 25 CpD resolution already suffices to resolve the physics involved in that phenomena.

- (2) *Far wake behavior converges with higher resolution:* The impact of finer resolutions becomes evident in the far wake of the helix cases, where the mean kinetic energies follow different trajectories for the different grid resolutions. With increasing resolution, their trajectories converge to the same trajectory. The finer grids also resolve the smaller structures, so less energy must be modeled with the sub-grid model. The most interesting phenomena occur in regions 1 and 2 up to around  $x = 3 - 4D$ , following the subdivision introduced in Fig. 12. The close trajectories of 50 and 80 CpD cases in this region and even further confirm that the relevant phenomena are sufficiently resolved.
- (3) *In the baseline case, the onset of the wake recovery moves upstream for higher resolutions:* The baseline case behaves differently from the helix cases, where the dominant driver for the transition from near wake to far wake is the breakdown of the tip vortices. In atmospheric flows, an initial perturbation induced by the inflow turbulence grows to trigger mutual instabilities between neighboring tip-vortices, causing them to pair and break down. Laminar inflow lacks that initial trigger for the tip-vortex instabilities; hence, the tip vortices remain stable over a long streamwise distance. For instance, Ivanell *et al.*<sup>62</sup> and Sarmast *et al.*<sup>63</sup> studied a wind turbine in laminar inflow using the fourth-order spectral Navier–Stokes solver in a one-third rotor domain resolved with 140 CpD without observing a tip vortex breakdown until  $x = 9.25 D$ . Only by introducing a low-amplitude body force excitation at the blades the tip vortex instability was triggered.

The lower-order scheme and the necessity of a full rotor domain and the lack of an initial perturbation imply that we cannot expect to resolve the classic tip-vortex breakdown in our baseline

simulations. Instead, the tip vortices vanish into a shear layer due to the numerical diffusion, which then breaks down in a Kelvin–Helmholtz-like shear layer instability as visible in Fig. 6. The grid convergence study reveals that the onset of that stability and the subsequent wake transition is not captured in the domain for the 25 CpD case and moves from  $x = 8.5D$  in the 50 CpD case to  $x = 5.5D$  in the 80 CpD resolution. It is assumed that the transition point of the baseline would move even further upstream with higher grid resolutions.

This implies that the baseline does not serve for quantitative performance comparisons with the helix cases in the far wake. The main focus of this work is to clarify the mechanisms in the helix wakes, particularly their differences in CW and CCW helix. The main reason for adding the baseline was to analyze the initial helix perturbation at the rotor in Sec. III A. and its qualitative effect on the near wake in Fig. 13. These comparisons can be made given the above-mentioned considerations.

## REFERENCES

- <sup>1</sup>P. Veers, K. Dykes, E. Lantz, S. Barth, C. L. Bottasso, O. Carlson, A. Clifton, J. Green, P. Green, H. Holtinen, D. Laird, V. Lehtomäki, J. K. Lundquist, J. Manwell, M. Marquis, C. Meneveau, P. Moriarty, X. Munduate, M. Muskulus, J. Naughton, L. Pao, J. Paquette, J. Peinke, A. Robertson, J. S. Rodrigo, A. M. Sempreviva, J. C. Smith, A. Tuohy, and R. Wiser, “Grand challenges in the science of wind energy,” *Science* **366**, eaau2027 (2019).
- <sup>2</sup>R. Barthelmie, S. Pryor, S. Frandsen, K. S. Hansen, J. Schepers, K. Rados, W. Schlez, A. Neubert, L. Jensen, and S. Neckelmann, “Quantifying the impact of wind turbine wakes on power output at offshore wind farms,” *J. Atmos. Oceanic Technol.* **27**, 1302–1317 (2010).
- <sup>3</sup>J. Meyers, C. Bottasso, K. Dykes, P. Fleming, P. Gebraad, G. Giebel, T. Göçmen, and J.-W. van Wingerden, “Wind farm flow control: Prospects and challenges,” *Wind Energy Sci.* **7**, 2271–2306 (2022).
- <sup>4</sup>E. Bossanyi and R. Ruisi, “Axial induction controller field test at sedini wind farm,” *Wind Energy Sci.* **6**, 389–408 (2021).
- <sup>5</sup>P. M. O. Gebraad, F. W. Teeuwisse, J. W. van Wingerden, P. A. Fleming, S. D. Ruben, J. R. Marden, and L. Y. Pao, “Wind plant power optimization through yaw control using a parametric model for wake effects—A CFD simulation study,” *Wind Energy* **19**, 95–114 (2016).
- <sup>6</sup>M. Bastankhah and F. Porté-Agel, “Wind farm power optimization via yaw angle control: A wind tunnel study,” *J. Renewable Sustainable Energy* **11**, 023301 (2019).
- <sup>7</sup>B. M. Doekemeijer, S. Kern, S. Maturu, S. Kanev, B. Salbert, J. Schreiber, F. Campagnolo, C. L. Bottasso, S. Schuler, F. Wils, T. Neumann, G. Potenza, F. Calabretta, F. Fioretti, and J.-W. van Wingerden, “Field experiment for open-loop yaw-based wake steering at a commercial onshore wind farm in Italy,” *Wind Energy Sci.* **6**, 159–176 (2021).
- <sup>8</sup>P. Fleming, J. King, E. Simley, J. Roadman, A. Scholbrock, P. Murphy, J. K. Lundquist, P. Moriarty, K. Fleming, J. van Dam, C. Bay, R. Mudafort, D. Jager, J. Skopek, M. Scott, B. Ryan, C. Guernsey, and D. Brake, “Continued results from a field campaign of wake steering applied at a commercial wind farm—Part 2,” *Wind Energy Sci.* **5**, 945–958 (2020).
- <sup>9</sup>W. Munter and J. Meyers, “An optimal control framework for dynamic induction control of wind farms and their interaction with the atmospheric boundary layer,” *Phil. Trans. R. Soc. A* **375**, 20160100 (2017).
- <sup>10</sup>W. Munter and J. Meyers, “Towards practical dynamic induction control of wind farms: Analysis of optimally controlled wind-farm boundary layers and sinusoidal induction control of first-row turbines,” *Wind Energy Sci.* **3**, 409–425 (2018).
- <sup>11</sup>J. A. Frederik, B. M. Doekemeijer, S. P. Mulders, and J.-W. van Wingerden, “The helix approach: Using dynamic individual pitch control to enhance wake mixing in wind farms,” *Wind Energy* **23**, 1739–1751 (2020).
- <sup>12</sup>E. Taschner, A. van Vondelen, R. Verzijlbergh, and J. van Wingerden, “On the performance of the helix wind farm control approach in the conventionally neutral atmospheric boundary layer,” *J. Phys.: Conf. Ser.* **2505**, 012006 (2023).

- <sup>13</sup>D. V. D. Hoek, C. S. Ferreira, and J.-W. V. Wingerden, "Experimental comparison of induction control methods for wind farm power maximization on a scaled two-turbine setup," *J. Phys.: Conf. Ser.* **2767**, 092064 (2024).
- <sup>14</sup>E. Taschner, M. Becker, R. Verzijlbergh, and J. V. Wingerden, "Comparison of helix and wake steering control for varying turbine spacing and wind direction," *J. Phys.: Conf. Ser.* **2767**, 032023 (2024).
- <sup>15</sup>C. Muscari, P. Schito, A. Viré, A. Zasso, D. van der Hoek, and J. van Wingerden, "Physics informed DMD for periodic dynamic induction control of wind farms," *J. Phys.: Conf. Ser.* **2265**, 022057 (2022).
- <sup>16</sup>M. Coquelet, J. Gutknecht, J. V. Wingerden, M. Duponcheel, and P. Chatelain, "Dynamic individual pitch control for wake mitigation: Why does the helix handedness in the wake matter?," *J. Phys.: Conf. Ser.* **2767**, 092084 (2024).
- <sup>17</sup>D. van der Hoek, B. V. den Abbeele, C. S. Ferreira, and J.-W. van Wingerden, "Maximizing wind farm power output with the helix approach: Experimental validation and wake analysis using tomographic particle image velocimetry," *Wind Energy* **27**, 463–482 (2024).
- <sup>18</sup>F. V. Mühle, F. M. Heckmeier, F. Campagnolo, and C. Breitsamter, "Wind tunnel investigations of an individual pitch control strategy for wind farm power optimization," *Wind Energy Sci.* **9**, 1251–1271 (2024).
- <sup>19</sup>A. A. Van Vondelen, S. T. Navalkar, D. R. Kerssemakers, and J.-W. Van Wingerden, "Enhanced wake mixing in wind farms using the helix approach: A loads sensitivity study," in *Proceedings of the 2023 American Control Conference (ACC)* (IEEE, 2023), pp. 831–836.
- <sup>20</sup>H. Korb, H. Asmuth, and S. Ivanell, "The characteristics of helically deflected wind turbine wakes," *J. Fluid Mech.* **965**, A2 (2023).
- <sup>21</sup>M. F. Howland, J. Bossuyt, L. A. Martínez-Tossas, J. Meyers, and C. Meneveau, "Wake structure in actuator disk models of wind turbines in yaw under uniform inflow conditions," *J. Renewable Sustainable Energy* **8**, 043301 (2016).
- <sup>22</sup>K. Brown, G. Yalla, L. Cheung, J. Frederik, D. Houck, N. deVelder, E. Simley, and P. Fleming, "Comparison of wind-farm control strategies under realistic offshore wind conditions: Wake quantities of interest," *Wind Energy Sci. Discuss.* **2025**, 1–39.
- <sup>23</sup>J. Gutknecht, D. van den Berg, D. van der Hoek, B. de Vos, B. Harder, A. Viré, and J. van Wingerden, "Wake recovery enhancement with helix active wake control: Vortex structures in a porous disk wake observed in PIV experiments," *J. Phys.: Conf. Ser.* **3016**, 012030 (2025).
- <sup>24</sup>J. Gutknecht, M. Becker, C. Muscari, T. Lutz, and J.-W. v. Wingerden, "Scaling DMD modes for modeling dynamic induction control wakes in various wind speeds," in *Proceedings of the 2023 IEEE Conference on Control Technology and Applications (CCTA)* (IEEE, 2023), pp. 574–580.
- <sup>25</sup>L. C. Cheung, K. A. Brown, D. R. Houck, and N. B. deVelder, "Fluid-dynamic mechanisms underlying wind turbine wake control with Strouhal-timed actuation," *Energies* **17**, 865 (2024).
- <sup>26</sup>J. Jonkman, S. Butterfield, W. Musial, and G. Scott, "Definition of a 5-mw reference wind turbine for offshore system development," Technical Report No. 947422, 2009.
- <sup>27</sup>M. A. Sprague, S. Ananthan, G. Vijayakumar, and M. Robinson, "ExaWind: A multifidelity modeling and simulation environment for wind energy," *J. Phys.: Conf. Ser.* **1452**, 012071 (2020).
- <sup>28</sup>M. B. Kuhn, M. T. Henry de Frahan, P. Mohan, G. Deskos, M. Churchfield, L. Cheung, A. Sharma, A. Almgren, S. Ananthan, M. J. Brazell, L. A. Martínez-Tossas, R. Thedin, J. Rood, P. Sakievich, G. Vijayakumar, W. Zhang, and M. Sprague, "AMR-wind: A performance-portable, high-fidelity flow solver for wind farm simulations," *Wind Energy* **28**, e70010 (2025).
- <sup>29</sup>J. Jonkman, "The new modularization framework for the fast wind turbine CAE tool," in *Proceedings of the 51st AIAA Aerospace Sciences Meeting Including the New Horizons Forum and Aerospace Exposition* (2013).
- <sup>30</sup>J. Smagorinsky, "General circulation experiments with the primitive equations: I. The basic experiment," *Mon. Weather Rev.* **91**, 99–164 (1963).
- <sup>31</sup>A. S. Almgren, J. B. Bell, P. Colella, L. H. Howell, and M. L. Welcome, "A conservative adaptive projection method for the variable density incompressible Navier–Stokes equations," *J. Comput. Phys.* **142**, 1–46 (1998).
- <sup>32</sup>L. Martinez, S. Leonardi, M. Churchfield, and P. Moriarty, "A comparison of actuator disk and actuator line wind turbine models and best practices for their use," in *Proceedings of the 50th AIAA Aerospace Sciences Meeting Including the New Horizons Forum and Aerospace Exposition* (2012).
- <sup>33</sup>N. Trolldborg, J. N. Sorensen, and R. Mikkelsen, "Numerical simulations of wake characteristics of a wind turbine in uniform inflow," *Wind Energy* **13**, 86–99 (2010).
- <sup>34</sup>S. Ivanell, J. N. Sørensen, R. Mikkelsen, and D. Henningson, "Analysis of numerically generated wake structures," *Wind Energy* **12**, 63–80 (2009).
- <sup>35</sup>M. J. Churchfield, S. Lee, J. Michalakes, and P. J. Moriarty, "A numerical study of the effects of atmospheric and wake turbulence on wind turbine dynamics," *J. Turbul.* **13**, N14 (2012).
- <sup>36</sup>J. N. Sorensen and W. Z. Shen, "Numerical modeling of wind turbine wakes," *J. Fluids Eng.* **124**, 393–399 (2002). See [https://asmedigitalcollection.asme.org/fluidengineering/article-pdf/124/2/393/5678518/393\\_1.pdf](https://asmedigitalcollection.asme.org/fluidengineering/article-pdf/124/2/393/5678518/393_1.pdf).
- <sup>37</sup>N. J. Abbas, D. S. Zalkind, L. Pao, and A. Wright, "A reference open-source controller for fixed and floating offshore wind turbines," *Wind Energy Sci.* **7**, 53–73 (2022).
- <sup>38</sup>A. K. M. F. Hussain and W. C. Reynolds, "The mechanics of an organized wave in turbulent shear flow," *J. Fluid Mech.* **41**, 241–258 (1970).
- <sup>39</sup>W. C. Reynolds and A. K. M. F. Hussain, "The mechanics of an organized wave in turbulent shear flow. Part 3. Theoretical models and comparisons with experiments," *J. Fluid Mech.* **54**, 263–288 (1972).
- <sup>40</sup>R. B. Cal, J. Lebrón, L. Castillo, H. S. Kang, and C. Meneveau, "Experimental study of the horizontally averaged flow structure in a model wind-turbine array boundary layer," *J. Renewable Sustainable Energy* **2**, 013106 (2010).
- <sup>41</sup>M. Calaf, C. Meneveau, and J. Meyers, "Large eddy simulation study of fully developed wind-turbine array boundary layers," *Phys. Fluids* **22**, 015110 (2010).
- <sup>42</sup>F. Houtin-Mongrolle, P. Benard, G. Lartigue, and V. Moureau, "A level-set framework for the wind turbine wake analysis: From high-fidelity unsteady simulations to 1D momentum theory," *J. Phys.: Conf. Ser.* **1934**, 012011 (2021).
- <sup>43</sup>L. Lignarolo, D. Ragni, F. Scarano, C. Simão Ferreira, and G. van Bussel, "Tip-vortex instability and turbulent mixing in wind-turbine wakes," *J. Fluid Mech.* **781**, 467–493 (2015).
- <sup>44</sup>J. M. Wallace, H. Eckelmann, and R. S. Brodkey, "The wall region in turbulent shear flow," *J. Fluid Mech.* **54**, 39–48 (1972).
- <sup>45</sup>L. A. Martínez-Tossas, M. J. Churchfield, A. E. Yilmaz, H. Sarlak, P. L. Johnson, J. N. Sørensen, J. Meyers, and C. Meneveau, "Comparison of four large-eddy simulation research codes and effects of model coefficient and inflow turbulence in actuator-line-based wind turbine modeling," *J. Renewable Sustainable Energy* **10**, 033301 (2018).
- <sup>46</sup>J. C. Hunt, A. A. Wray, and P. Moin, "Eddies, streams, and convergence zones in turbulent flows," in *Studying Turbulence Using Numerical Simulation Databases*, 2. Proceedings of the 1988 Summer Program (1988).
- <sup>47</sup>R. Pain, P.-E. Weiss, S. Deck, and J.-C. Robinet, "Large scale dynamics of a high Reynolds number axisymmetric separating/reattaching flow," *Phys. Fluids* **31**, 125119 (2019).
- <sup>48</sup>R. Soto-Valle, S. Cioni, S. Bartholomay, M. Manolesos, C. N. Nayeri, A. Bianchini, and C. O. Paschereit, "Vortex identification methods applied to wind turbine tip vortices," *Wind Energy Sci.* **7**, 585–602 (2022).
- <sup>49</sup>S. G. Horcas, T. Barlas, F. Zahle, and N. N. Sørensen, "Vortex induced vibrations of wind turbine blades: Influence of the tip geometry," *Phys. Fluids* **32**, 065104 (2020).
- <sup>50</sup>T. Leweke, S. Le Dizès, and C. H. Williamson, "Dynamics and instabilities of vortex pairs," *Annu. Rev. Fluid Mech.* **48**, 507–541 (2016).
- <sup>51</sup>P. Meunier, U. Ehrenstein, T. Leweke, and M. Rossi, "A merging criterion for two-dimensional co-rotating vortices," *Phys. Fluids* **14**, 2757–2766 (2002). See [https://pubs.aip.org/aip/pof/article-pdf/14/8/2757/19308925/2757\\_1\\_online.pdf](https://pubs.aip.org/aip/pof/article-pdf/14/8/2757/19308925/2757_1_online.pdf).
- <sup>52</sup>D. M. Harris and C. H. K. Williamson, "Instability of secondary vortices generated by a vortex pair in ground effect," *J. Fluid Mech.* **700**, 148–186 (2012).
- <sup>53</sup>P. Meunier and T. Leweke, "Elliptic instability of a co-rotating vortex pair," *J. Fluid Mech.* **533**, 125–159 (2005).
- <sup>54</sup>F. Laporte and A. Corjon, "Direct numerical simulations of the elliptic instability of a vortex pair," *Phys. Fluids* **12**, 1016–1031 (2000). See [https://pubs.aip.org/aip/pof/article-pdf/12/5/1016/19223765/1016\\_1\\_online.pdf](https://pubs.aip.org/aip/pof/article-pdf/12/5/1016/19223765/1016_1_online.pdf).
- <sup>55</sup>T. Leweke and C. H. K. Williamson, "Cooperative elliptic instability of a vortex pair," *J. Fluid Mech.* **360**, 85–119 (1998).
- <sup>56</sup>M. Bastankhah and F. Porté-Agel, "Experimental and theoretical study of wind turbine wakes in yawed conditions," *J. Fluid Mech.* **806**, 506–541 (2016).

- <sup>57</sup>C. R. Shapiro, D. F. Gayme, and C. Meneveau, "Generation and decay of counter-rotating vortices downstream of yawed wind turbines in the atmospheric boundary layer," *J. Fluid Mech.* **903**, R2 (2020).
- <sup>58</sup>A. A. W. van Vondelen, A. K. Pamososuryo, S. T. Navalkar, and J.-W. van Wingerden, "Control of periodically waked wind turbines," *IEEE Trans. Control Syst. Technol.* **33**, 700 (2025).
- <sup>59</sup>Dvd Berg, Dd Tavernier, and v Wingerden, "Using The Helix Mixing Approach On Floating Offshore Wind Turbines," *J. Phys: Conf. Ser.* (2022). 2265(4), 042011
- <sup>60</sup>J. Gutknecht, A. van den Homberg, J. Linke, J. van der Marel, J. van der Meulen, R. Hendriks, A. Viré, and J. van Wingerden, "Synergizing helix active wake mixing with dynamic yawing: An exploration study using porous discs in a wind tunnel," *J. Phys.: Conf. Ser.* 3016, 012014.
- <sup>61</sup>L. A. Martínez-Tossas, J. Annoni, P. A. Fleming, and M. J. Churchfield, "The aerodynamics of the curled wake: A simplified model in view of flow control," *Wind Energy Sci.* **4**, 127–138 (2019).
- <sup>62</sup>S. Ivanell, R. Mikkelsen, J. N. Sørensen, and D. Henningson, "Stability analysis of the tip vortices of a wind turbine," *Wind Energy* **13**, 705–715 (2010).
- <sup>63</sup>S. Sarmast, R. Dadfar, R. F. Mikkelsen, P. Schlatter, S. Ivanell, J. Sørensen, and D. Henningson, "Mutual inductance instability of the tip vortices behind a wind turbine," *J. Fluid Mech.* **755**, 705–731 (2014).